A&A 580, A36 (2015)
DOI: 10.1051/0004-6361/201525990

Astronomy & Astrophysics

ALMA observations of TiO_2 around VY Canis Majoris⋆

E. De Beck[1], W. Vlemmings[1], S. Muller[1], J. H. Black[1], E. O'Gorman[1], A. M. S. Richards[2], A. Baudry[3,4], M. Maercker[1], L. Decin[5,6], and E. M. Humphreys[7]

[1] Department of Earth and Space Sciences, Chalmers University of Technology, Onsala Space Observatory, 43992 Onsala, Sweden
e-mail: elvire.debeck@chalmers.se
[2] Jodrell Bank Centre for Astrophysics, School of Physics and Astronomy, University of Manchester, Manchester M13 9PL, UK
[3] Université de Bordeaux, LAB, UMR 5804, 33270 Floirac, France
[4] CNRS, LAB, UMR 5804, 33270 Floirac, France
[5] Instituut voor Sterrenkunde, Katholieke Universiteit Leuven, Celestijnenlaan 200D, 3001 Leuven, Belgium
[6] Sterrenkundig Instituut Anton Pannekoek, University of Amsterdam, Science Park 904, 1098 Amsterdam, The Netherlands
[7] European Southern Observatory, Karl-Schwarzschild-Straße 2, 85748 Garching, Germany

Received 28 February 2015 / Accepted 25 May 2015

ABSTRACT

Context. Titanium dioxide, TiO_2, is a refractory species that could play a crucial role in the dust-condensation sequence around oxygen-rich evolved stars. To date, gas phase TiO_2 has been detected only in the complex environment of the red supergiant VY CMa.
Aims. We aim to constrain the distribution and excitation of TiO_2 around VY CMa in order to clarify its role in dust formation.
Methods. We analyse spectra and channel maps for TiO_2 extracted from ALMA science verification data.
Results. We detect 15 transitions of TiO_2, and spatially resolve the emission for the first time. The maps demonstrate a highly clumpy, anisotropic outflow in which the TiO_2 emission likely traces gas exposed to the stellar radiation field. An accelerating bipolar-like structure is found, oriented roughly east-west, of which the blue component runs into and breaks up around a solid continuum component. A distinct tail to the south-west is seen for some transitions, consistent with features seen in the optical and near-infrared.
Conclusions. We find that a significant fraction of TiO_2 remains in the gas phase outside the dust-formation zone and suggest that this species might play only a minor role in the dust-condensation process around extreme oxygen-rich evolved stars like VY CMa.

Key words. supergiants – stars: individual: VY Canis Majoris – stars: mass-loss – circumstellar matter – submillimeter: stars

1. Introduction

The dust-formation sequence in the outflows of oxygen-rich evolved stars is not well understood. It is essential to address which gas-phase species provide the primary seeds. TiO_2 is considered an important seed refractory species with possibly higher nucleation rates than SiO (e.g. Jeong et al. 2003; Lee et al. 2015). Moreover, presolar TiO_2 grains were tentatively identified by Nittler & Alexander (1999). Since SiO nucleation was recently indicated to be more relevant than previously thought under the relevant pressure and temperature conditions (Nuth & Ferguson 2006; Gail et al. 2013), it is crucial to characterise the role of TiO_2. The effect of non-stationarity on the nucleation is unknown. Shocks are, however, known to be present in the upper atmospheres of these evolved stars (e.g. Chiavassa et al. 2011).

Emission from gas phase TiO_2 has only been detected towards VY CMa (Kamiński et al. 2013a,b, hereafter K+13a, K+13b). The circumstellar environment of this red supergiant (at 1.2 kpc; Zhang et al. 2012) exhibits a high degree of morphological complexity, from optical to radio wavelengths and on spatial scales from a few to several thousand AU (e.g. Humphreys et al. 2007; Kamiński et al. 2013b; Monnier et al. 2014; Muller et al. 2007; Shenoy et al. 2013; Smith et al. 2001; Ziurys et al. 2007). Recent ALMA observations spatially resolve H_2O maser emission, leading to the most accurate determination of the stellar position (Richards et al. 2014, hereafter R+14). O'Gorman et al. (2015, hereafter O+15) describe the submillimeter continuum emission and report on a bright component south-east of the star, indicative of anisotropic mass loss.

TiO_2 is expected to be consumed by the nucleation process, but the detection of TiO_2 emission by K+13a already suggested that a significant amount could possibly survive the dust formation. K+13a did not spatially resolve TiO_2 emission at angular resolutions $\gtrsim 1''$. The ALMA observations now allow us to characterise the emission and the role of TiO_2 in the dust-formation process in more detail.

2. Observations

We retrieved ALMA science verification data on VY CMa from the ALMA archives. The observations and data calibration and reduction are described by R+14. Table 1 shows the spectral coverage and representative rms noise values for the six spectral windows in ALMA's band 7 (~0.9 mm; ~320 GHz) and one in band 9 (~0.45 mm; ~660 GHz). With projected baselines of 14 m up to 2.7 km, the spatial resolution at ~320 GHz and 658 GHz is ~0.″2 and ~0.″1, respectively, and the maximum recoverable scales are 8.″3 and 4.″0. The synthesised beam sizes are obtained using natural weighting.

The data reduction and quality of the continuum emission images at 321 GHz and 658 GHz are discussed in detail by R+14 and O+15. No imaging artefacts are expected to arise from the

⋆ Appendix A is available in electronic form at http://www.aanda.org

Table 1. Spectral coverage of the ALMA observations.

Setting	Frequency range (GHz)	Resolution (MHz)	rms noise (mJy beam^{-1})	Beam ("×", PA)
321	309.501−310.437	0.98	3	0.23 × 0.13, 28.27°
321	310.501−311.437	0.98	2	0.23 × 0.13, 28.48°
325	312.035−313.908	1.9	3	0.24 × 0.13, 29.48°
321	320.725−321.662	0.98	3	0.22 × 0.13, 27.31°
321	321.986−322.923	0.98	3	0.22 × 0.13, 27.55°
325	324.181−326.054	1.9	6	0.22 × 0.12, 29.27°
658	657.002−658.873	3.9	15	0.11 × 0.06, 29.89°

Notes. Setting names refer to those used for the released ALMA CSV data, focussing on the H_2O masers at 321 GHz, 325 GHz, and 658 GHz.

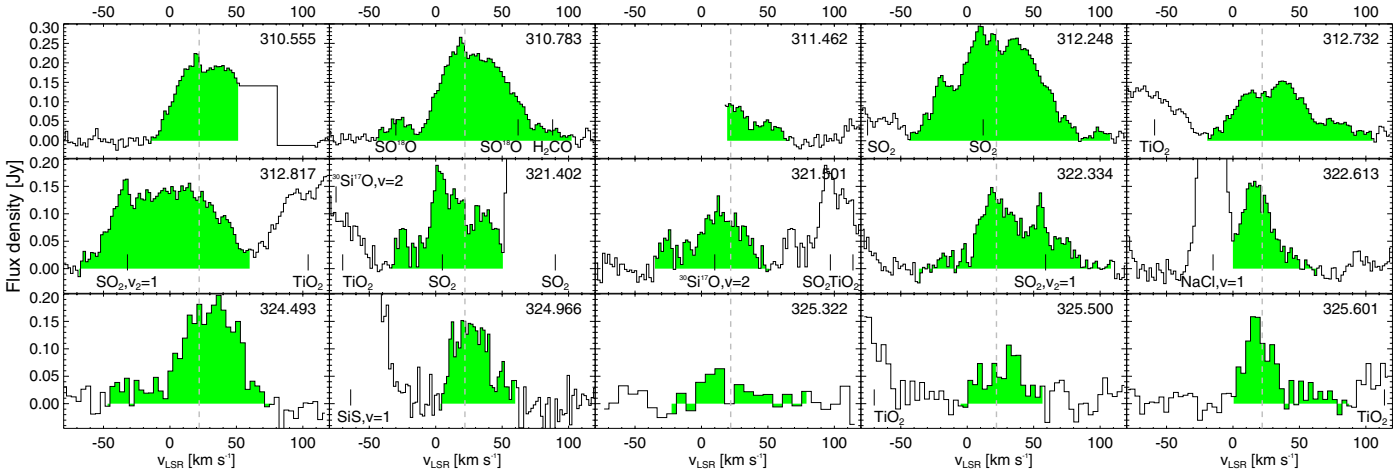

Fig. 1. TiO_2 spectra extracted for a 1″ diameter aperture around the stellar position. The vertical dashed lines indicate the stellar v_{LSR} of 22 km s^{-1}, the shaded areas the v_{LSR}-ranges from Table 2. We indicate identifications of species other than TiO_2 in the panels.

array configuration owing to the excellent coverage of the visibility plane.

We note that the spectral window 312−314 GHz suffered from poor continuum subtraction owing to line crowding and a consequent lack of line-free spectral range. This causes a fraction of the continuum emission to leak into the channel maps of the TiO_2 lines at ∼312 GHz (Figs. A.4–A.6). The emission seen at the position of clump C can be entirely attributed to the continuum itself, i.e. we can rule out molecular contribution at this position. The lines presented in Fig. 1 and Table 2, and consequently also the reported peak and integrated intensities, were corrected for this effect on a line-to-line basis.

The imaged TiO_2 lines in the 312−314 GHz spectral window also show a contribution north-north-east and south-south-west of the star. These features are artefacts of the cleaning procedure likely caused by imperfect phase corrections on a number of intermediate baselines. The phase corrections were transferred from the self-calibrated 325 GHz maser line located in the atmospheric absorption region.

3. Results

We analysed spectra extracted for a 1″ diameter region around the stellar position. We show below that no TiO_2 emission is detected beyond this aperture. TiO_2 identifications are based on the Cologne Database for Molecular Spectroscopy (CDMS; Müller et al. 2001, 2005; Brünken et al. 2008). We detect 15 lines with upper-level energies E_{up}/k in the range 48−676 K and signal-to-noise ratios $S/N \approx 5$−17 at velocity resolutions 0.9−7.6 km s^{-1} (Table 2, Fig. 1). Of the TiO_2 lines detected by K+13a; K+13b only those at 310.55 GHz and 310.78 GHz are observed with ALMA. The peak fluxes of the ALMA and SMA detections are consistent within the uncertainties. Moreover, of the other 13 lines of TiO_2 detected with ALMA, none were detected in the SMA survey, owing to a noise level in the ALMA data that was approximately 10 times lower. We detect no TiO_2 emission at ∼660 GHz owing to the higher rms noise (Table 1). We detect no isotopic variants of Ti, consistent with the solar isotopic abundance ratios.

We expect no large flux losses in the ALMA observations of TiO_2, given the ∼8″ recoverable scale at ∼320 GHz. The presence of large-scale emission with low surface brightness cannot be entirely excluded, but is unlikely and will not change our main conclusions.

Blending, proximity to strong lines, line crowding, and intrinsic line-shape irregularities complicate the identification of TiO_2 emission. The lines at 310.55 GHz and 311.46 GHz are only partially covered in the observations; we believe the former to be a firm detection and the latter to be tentative. In both cases, no other candidate could be identified. Uncertainties on the relevant TiO_2 frequencies are <2 MHz, except for the transition at 311.462 GHz, where it is 5.555 MHz (Brünken et al. 2008).

The TiO_2 lines detected with ALMA exhibit broad line profiles, as do those detected by K+13a. Assuming[1] a stellar v_{LSR} of 22 km s^{-1}, we find that the emission is very asymmetric in velocity space, ranging typically from ∼−15 km s^{-1} to ∼60 km s^{-1} (Fig. 1). The apparent extension of the blue wing of some lines to ∼−45 km s^{-1} is likely coincidental and due to line blending, but

[1] See K+13b for a discussion of v_{LSR}.

Table 2. Overview of detected TiO_2 lines.

Transition $J'_{K'_a,K'_c}-J_{K_a,K_c}$	ν_{lab} (MHz)	E_{up}/k (K)	v_{min}	v_{max} (km s^{-1})	Δv	rms (mJy)	Peak (Jy)	I (Jy km s^{-1})	Size ($''$)	SW tail
22(1, 21)−21(2, 20)	310 554.735	180.5	−15.2	51.3	1.0	16	0.22	9.57	0.9	Y
23(1, 23)−22(0, 22)	310 782.713	182.4	−43.9	102.3	1.0	16	0.27	15.28	0.9	Y
40(8, 32)−39(9, 31)	311 462.082	675.9	19.4	66.7	1.9	10	0.10	2.31	0.8	–
7(5, 3)−6(4, 2)	312 248.341	47.9	−43.7	80.96	1.9	16	0.29	20.32	0.8	N
10(4, 6)−9(3, 7)	312 732.066	57.7	−19.4	105.1	1.9	16	0.15	9.43	0.5	?
30(3, 27)−30(2, 28)	312 816.809	354.4	−68.2	60.0	1.9	16	0.16	12.98	0.5	?
11(4, 8)−10(3, 7)	321 401.936	65.7	−33.9	50.5	0.9	24	0.19	7.24	0.8	?
28(2, 26)−28(1, 27)	321 501.043	298.8	−35.0	51.2	0.9	24	0.13	4.76	0.9	N
35(8, 28)−35(7, 29)	322 333.594	532.4	−36.4	108.1	1.0	19	0.15	7.03	0.8	N
33(8, 26)−33(7, 27)	322 612.696	481.4	−0.1	63.9	1.0	18	0.16	4.18	0.9	N
23(2, 22)−22(1, 21)	324 492.930	196.1	−47.9	79.4	1.9	29	0.21	9.64	$\lesssim$0.5	N
37(8, 30)−37(7, 31)	324 965.693	586.5	3.6	59.8	1.9	30	0.15	4.92	0.5	N
26(1, 25)−26(0, 26)	325 322.035	246.5	−25.2	81.8	7.6	21	0.11	1.85	0.5	N
26(4, 22)−25(5, 21)	325 500.415	281.5	−7.7	55.7	3.8	28	0.13	2.75	0.5	N
28(8, 20)−28(7, 21)	325 600.792	367.0	−0.4	90.2	3.8	28	0.18	3.89	0.5	N

Notes. Parameters listed for spectrum extracted in a 1″ diameter aperture centred on the star. See also Fig. 1. Columns are transition, rest frequency, upper-level energy, minimum and maximum v_{LSR} reached, velocity resolution and rms noise at which the identification was made, peak and integrated flux, maximum diametric size of the integrated emission at 3σ level, and a marker for emission in the south-west tail (Y, N, ?, and – for yes, no, maybe, and unknown). Species other than TiO_2 detected inside the plotted spectral windows are marked in Fig. 1.

we cannot exclude an actual TiO_2 contribution. Blend candidates are indicated in Fig. 1 and Table 2. The lines with E_{up}/k = 48 K[2], 58 K, 182 K, 532 K exhibit features in their red wings that extend to $v_{LSR} \approx 105$ km s^{-1}. A similar high-velocity outflow is also visible for some lines presented by K+13a.

3.1. Spatial distribution

The detected TiO_2 emission is, for the most part, spatially resolved by the ALMA observations with a 0.″23 × 0.″13 beam (see Figs. A.1–A.16), but several transitions show spatially unresolved emission at a 2 km s^{-1} velocity resolution. We note a very complex behaviour of the emission peaks, with some only appearing in one channel and not in the neighbouring channels. The often spatially unresolved ($\lesssim$145 AU) peaks in the different velocity channels of all lines imply a clumpy and/or anisotropic wind. The maps for 310.55 GHz (E_{up}/k = 181 K) and 310.78 GHz (E_{up}/k = 182 K) reveal that these two lines behave almost identically. Corresponding velocity channels (Figs. A.1, A.2) trace roughly the same regions of the circumstellar environment and exhibit similar intensities, implying that these two lines are very tightly coupled in their excitation. Figure 2 shows the morphology of the TiO_2 emission at 310.78 GHz and the positions of the star (VY), the continuum component C (O+15; R+14), and the south-west clump detected at $\lambda \sim 1$–5 μm at ∼1″ from the star (Smith et al. 2001; Humphreys et al. 2007; Shenoy et al. 2013).

Given the similar energy levels, quantum numbers, and Einstein-A coefficients of the transitions at 310.55 GHz, 310.78 GHz, and 324.49 GHz, one expects similar line intensities and spatial distributions. However, although the channel-to-channel peaks of the 324.49 GHz emission (Fig. A.11) correspond quite well to those of the other two, which strengthens its identification as TiO_2, its intensity is clearly lower. It is hard to explain this discrepancy, but we note that as a consequence of the sensitivity of the atmospheric transmission at ∼325 GHz to the atmospheric water-vapour content the rms noise is ∼4 times higher and the flux calibration could be compromised.

The emission at 322.61 GHz, 322.33 GHz, and 324.96 GHz behaves similarly but with weaker and spatially somewhat more confined red-wing emission. Unfortunately, many of the TiO_2 lines are blended (both in frequency and spatially) with emission from other species.

The discussion below is focussed on the morphology at 310.78 GHz with Fig. 2 as a visual guide. Overall, the detected TiO_2 emission moves from west to east, across the stellar position, with velocities evolving from reddest to bluest. All lines show emission close to the star at the stellar v_{LSR}. In particular, all lines with $E_{up}/k \gtrsim 360$ K are centred on VY and emit mainly across $v_{LSR} \approx 0$–40 km s^{-1} (Fig. 1), implying that these trace a central part of the outflow that may be accelerating.

At $v_{LSR} \geq 44$ km s^{-1} the emission is mainly situated west of VY with a marginal contribution close to it. The emission is highly variable with v_{LSR}, doubly peaked in most velocity channels, and shows a hook-like feature at its western edge. The latter could relate to the north-west knot defined by Humphreys et al. (2007) based on HST observations, though more analysis is needed to investigate the nature of this feature.

At $22 < v_{LSR} < 44$ km s^{-1} we find multiple emission peaks in most velocity channels, with those closest to VY slightly brighter than the west offset peaks. The integrated emission is elongated along a direction roughly parallel to the axis connecting the peak position of C and VY, at a PA ≈ 125°.

At $18 \leq v_{LSR} \leq 22$ km s^{-1} the transitions at ∼310 GHz show a bright tail extending south-west of VY at a PA ≈ 220°, i.e. almost perpendicular to the axis connecting VY and C. This tail reaches ∼1″ away from VY, out to the south-west clump of Shenoy et al. (2013) and agrees very well with the features detected by e.g. Smith et al. (2001) at wavelengths $\lambda \sim 1$–2.14 μm. The emission at 310.78 GHz extends slightly further south-west than that at 310.55 GHz. Since the most extended emission

[2] Continuum subtraction is hampered by the high line density. The red wing of the line is affected, but still shows the feature they have in common.

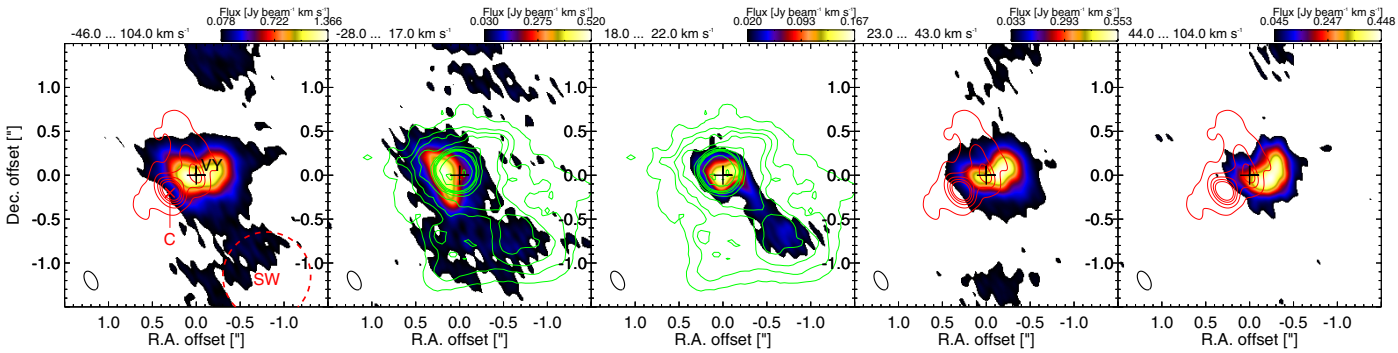

Fig. 2. TiO_2 morphology. Colour maps of emission at 310.78 GHz integrated over the v_{LSR}-ranges indicated at the top left of each panel, cut off at 3σ. Red contours show the 321 GHz continuum at [3, 20, 40, 60, 80]σ; green contours show HST emission at [3, 5, 7, 10, 20, 30, 40, 50, 100, 200]σ (Smith et al. 2001). In the *first panel* we mark the position of the star (+, VY; black) and of the continuum component (x, C; red) to the south-east (O+15; R+14), and the position and approximate extent of the south-west clump (SW, dashed 1″ diameter circle; red Shenoy et al. 2013). The apparent north-south emission is thought to arise from dynamic-range limitations in the peak channels.

exceeds 5σ, we suggest that the difference is real and that clumpiness in the outflow strongly influences the excitation of individual lines.

At 312.73 GHz and 312.82 GHz we find signs of emission in the south-west tail, but these are likely artefacts from the cleaning procedure (see Sect. 2). At 311.46 GHz we see emission within the spatial region where the wouth-west tail is located, although at higher v_{LSR} than the transitions at ~310 GHz. This could be due to the south-west tail covering a wider velocity range than reported above, by a line blend, or a misidentification of the line as TiO_2. We unfortunately do not have information for $v_{LSR} < 22$ km s^{-1} for this line. No other transition shows detectable emission within the south-west tail, but most show a slight bulge of emission at ~0.″2 south-west of the star, at the base of the south-west tail. Figure A.17 shows a comparison for all lines to the south-west tail observed at 310.78 GHz.

At $v_{LSR} < 18$ km s^{-1} the high-intensity emission is situated entirely east of VY, elongated, and oriented at ~15°–25° east from north. With bluer velocities the emission moves towards C and then appears to break up with a northern peak brighter than the southern one (e.g. Fig. A.2). Remarkable is that the low-intensity component of the 310.78 GHz transition closely resembles the scattered light at 1 μm. We find this strong correspondence at these blue velocities for no other TiO_2 transition. If the high- and low-intensity components have different intrinsic wind velocities, they could be spatially separated and trace different parts of the outflow.

3.2. Excitation conditions

We investigate the excitation of TiO_2 lines via a rotational diagram analysis (Fig. 3). Intensities, source sizes, and rms noise values are taken from Table 2. Severely blended or only partially covered lines are excluded from the analysis. We derive a source-averaged column density $N_{col} = 5.65 \pm 1.33 \times 10^{15}$ cm^{-2} and a rotational temperature $T_{rot} = 198.0 \pm 28.5$ K, in agreement with K+13a. We note that the kinetic temperature in the excitation region of TiO_2 varies from more than 1000 K down to ~100 K (Decin et al. 2006). Assuming an average mass-loss rate of 2×10^{-4} $M_\odot$ yr^{-1} (e.g. De Beck et al. 2010), an average velocity of 20 km s^{-1}, and an 0.″9 diametric extent, at 1.2 kpc, we find an abundance $TiO_2/H_2 \approx 3.8 \pm 0.9 \times 10^{-8}$.

The high dipole moment of TiO_2 (6.33 Debye; Wang et al. 2009) supports efficient radiative excitation and T_{rot} could hence

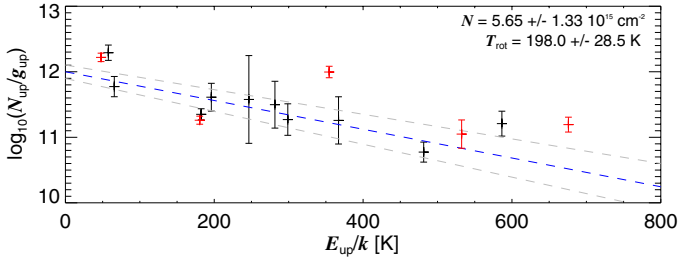

Fig. 3. Rotational diagram. Lines indicated in red are blended or only partially covered in the observations and are excluded from the fitting procedure. All intensities, source sizes, and rms noise values are taken from Table 2. The fit results and uncertainties are shown with the blue and grey dashed lines and are indicated at the top right.

reflect an average continuum brightness temperature as opposed to a gas kinetic temperature in the case of collisional excitation. Additionally, the large dipole moment induces electron-TiO_2 collision rates large enough to exceed H_2–TiO_2 collision rates if the fractional ionisation exceeds a few 10^{-6}. We could not find a value for VY CMa, but based on the result $n_e/n_H = 3.8 \times 10^{-4}$ for the red supergiant α Ori (Harper et al. 2001) this type of excitation could be relevant[3]. We discuss the competition between collisional excitation and radiative excitation in more detail below, in Sect. 4.1.

4. Discussion

4.1. Excitation of titanium dioxide

Many effects need to be taken into account in a full treatment of the excitation and radiative transfer of rotational transitions of TiO_2. Important molecular data are lacking: although the rotational energy levels and radiative data are well determined for TiO_2 in CDMS (Müller et al. 2001, 2005; Brünken et al. 2008), no rates exist for excitation of TiO_2 by hydrogen-impact nor have the vibration-rotation spectra been fully analysed.

For illustration of the transition rates for TiO_2, consider two of the observed rotational transitions at 312.248 and 324.965 GHz with properties summarised in Table 3. Collisional excitation at the kinetic temperature of the gas can dominate only when the downward rate of collision-induced transitions

[3] VY CMa is of spectral type M2.5-M5e Ia (Houk & Smith-Moore 1988), α Ori of spectral type M1-2Ia-ab (Keenan & McNeil 1989).

Table 3. Summary of properties of selected transitions of TiO_2.

$J'(K'_a, K'_c)$–$J''(K''_a, K''_c)$ or vibrational band	ν (GHz)	$A_{u,\ell}$ (s^{-1})	$\sum_\ell A_{u,\ell}$ (s^{-1})	n_0 (cm^{-3})	T_{rad} (K)	ρ_{rad} (s^{-1})
7(5, 3)–6(4, 2)	312.248	4.34×10^{-3}	5.04×10^{-3}	5×10^{7}	26.2	5.7×10^{-3}
7(5, 3)–7(4, 4)	206.094	6.95×10^{-4}	...	...	15.3	7.6×10^{-4}
7(5, 3)–8(4, 4)	84.567	7.31×10^{-6}	...	...	7.15	9.6×10^{-6}
37(8, 30)–37(7, 31)	324.966	4.76×10^{-3}	4.63×10^{-2}	5×10^{8}	27.7	6.3×10^{-3}
37(8, 30)–36(9, 27)	205.259	2.62×10^{-4}	...	...	15.2	2.9×10^{-4}
37(8, 30)–36(7, 29)	821.811	2.96×10^{-2}	...	...	94.3	5.7×10^{-2}
37(8, 30)–36(5, 31)	1235.577	1.17×10^{-2}	...	...	132.4	2.0×10^{-2}
$\nu_1 = 1$–0	28 840	3.6	3.6	[a]	350	7.2×10^{-2}
$\nu_2 = 1$–0	9863	7.2×10^{-2}	7.2×10^{-2}	[a]	300	2.0×10^{-2}
$\nu_3 = 1$–0	28 030	42	42	[a]	350	9.0×10^{-1}

Notes. Columns list the transitions (rotational and vibrational), the frequency ν at which these transitions occur, their transition probability $A_{u,\ell}$, inverse lifetime $\sum_\ell A_{u,\ell}$, critical density n_0, radiative temperature T_{rad} and the calculated pumping rate ρ_{rad}. [(a)] Appropriate collision rates are unknown; therefore, no critical density is tabulated for the vibrational transitions.

greatly exceeds the downward rates of radiative transitions for each upper state. This condition can be translated to a critical density $n_0 = \sum_\ell A_{u,\ell}/q_0$, where $A_{u,\ell}$ is the spontaneous transition probability of each transition from upper state u to lower state ℓ. To estimate this density, we assume a characteristic[4] quenching rate coefficient $q_0 = 10^{-10}$ cm^3 s^{-1} for rotational transitions induced by collisions with neutral species H or H_2. Values for n_0 are listed in Table 3. Assuming a mass-loss rate of 10^{-4} $M_\odot$ yr^{-1}, such densities are however reached only at distances from the star lower than ~0.″065, whereas TiO_2 is excited over a much larger region, where the density quickly decreases to a few 10^5 cm^{-3}.

In addition, collision rates for electron impact have been computed in the Born approximation. Because the electric dipole moment of TiO_2 is so large, electron-impact rates are expected to show a strong propensity for radiatively allowed transitions. Computed rates are likely to be accurate within 50%. Under an assumed very low fractional electron density of 10^{-7}, the collision-induced downward transition rate for the 312 GHz transition is for 5% due to electron collisions. Assuming the fractional ionisation reported for α Ori (3.8×10^{-4}) electron collisions would completely dominate over neutral (hydrogen) collisions by a factor of the order of 100 or more and might compete well with infrared pumping.

We note that the upper state of the 312 GHz transition decays mainly by the observed transition itself, while the upper state of the high-excitation 324 GHz transition is depopulated more rapidly by submm-wave transitions at 821 and 1235 GHz. As a consequence, a much higher density would be required to excite the 324 GHz line by collisions than the 312 GHz line.

The continuum intensity of VY CMa is so large at infrared and submm wavelengths that radiative excitation (pumping) must be taken into account. If the observed continuum flux of VY CMa is assumed to arise within a 0.″3 diameter region (O+15) and to be diluted by a geometrical factor 1/9 over the 0.″9 extent of the observed TiO_2 emission, then the average Planckian radiation brightness temperatures are estimated to be $T_{rad} \geq 25$ K at 312 to 324 GHz. The corresponding pumping rates (absorption and stimulated emission) in this radiation field can be expressed as

$$\rho_{rad} = \frac{A_{u,\ell}}{\exp(h\nu/kT_{rad}) - 1}$$

for each radiative transition that connects states of interest. The basic radiative data for TiO_2 are collected in Table 3. Although the fundamental bands of the three vibrational modes have not been fully analysed rotationally, the band frequencies and band strengths are approximately known (Grein 2007). In the adopted continuum model, the infrared intensity is high enough to drive absorption in vibration-rotation lines at rates of the order of 0.01 to 1.0 s^{-1}. In order for collisional excitation in a pure rotational transition $u \rightarrow \ell$ to compete with infrared pumping in VY CMa, a density much greater than

$$n_0 \approx \left(\rho(\nu_1) + \rho(\nu_2) + \rho(\nu_3) + \sum_\ell A_{u,\ell}\right)/q_0 \approx 10^{10} \quad cm^{-3}$$

would be required. The radiative rates in Table 3 suggest that radiative excitation is likely to be very important for TiO_2 in VY CMa. Therefore, the rotational temperature derived in Sect. 3.2 might have no direct relationship to the kinetic temperature. Because the observed transitions in the present study span a wide range of excitation energies, the simple rotation-diagram analysis still provides a useful first estimate of the molecular column density and abundance.

4.2. Outflow components

From the comparison to the continuum at ~321 GHz, we derive that TiO_2 is excited in the directions with lower dust densities. The absence of detected TiO_2 emission north of the star could then point to efficient obscuration of this part of the outflow, in line with the observations of e.g. Smith et al. (2001). Attenuation of the stellar radiation field to the east and west of the star is limited. From this, we do not expect an equatorial enhancement of the mass-loss rate, since this would likely have induced more efficient dust formation, which is not seen in the continuum.

The TiO_2 emission traces multiple wind components. We find a red outflow to the west and a blue outflow to the east. With the clear exception of the interaction of the TiO_2 gas with clump C in the east, the two seem roughly symmetric around the

[4] Such a value is typical of the largest downward collisional rates for H_2 collisions with a heavy, polar molecule. For example, accurate collision rates have been computed by Cernicharo et al. (2011) for H_2 on SO_2, a heavy molecule with a relatively large dipole moment (1.63 Debye). The SO_2 quenching rates at low temperature are $\sim 2 \times 10^{-10}$.

star and aligned with the axis connecting VY and C. We rule out an equatorially enhanced environment such as an expanding disk or ring, based on the spatial distribution of the TiO_2 emission at different v_{LSR}. We rather suggest an accelerating bipolar-like outflow at lower densities. We also find a predominantly blue south-west outflow, connecting the star and the south-west clump, approximately perpendicular to the VY – C connecting axis. We find no north-east counterpart in TiO_2 emission, likely implying that the south-west tail is indeed caused by an event in one preferred direction, as opposed to a bipolar event.

4.3. Interaction of blue outflow with clump C

Whereas the H_2O maser emission in the "valley" between VY and C implies that C is close to or in the plane of the sky (R+14), the observations suggest that the TiO_2 gas breaks up around C while moving towards the observer, placing C – at least partially – in front of the plane of the sky. We therefore deem it likely that the H_2O masers and the TiO_2 emission probe parts of the outflow east of VY with different physical properties. Whereas the masers are probably excited through shocks at high densities, TiO_2 is more likely excited through radiation, at lower outflow densities. In the denser regions, TiO_2 might not be excited and/or it might be efficiently depleted from the gas phase. The latter is, however, less likely (see below). We therefore suggest that TiO_2 traces the blue-shifted wind to the east of VY with lower densities which runs into and curves around C.

4.4. Titanium dioxide and scattered light

K+13b reported emission offset by ∼1″ south-west from the central molecular emission for multiple species. However, owing to lower sensitivity they did not find indications for this in the TiO_2 emission, whereas we clearly detect the south-west tail at ∼310 GHz (see Sect. 3.1).

The likelihood of radiative excitation of TiO_2 and the agreement between the south-west tail in the TiO_2 emission and the scattered stellar light at 1 μm from Smith et al. (2001) suggest the presence of a tail of gas and dust lit up by a stellar radiation field less attenuated than at other position angles. The bulge south-west of the star seen for most TiO_2 transitions is consistent with this. We infer a lower degree of attenuation and from that a lower (dust) density south-west of the star. We speculate that the suggested localised ejection leading to the formation of the south-west clump (Shenoy et al. 2013) could have created a cavity in the dense material close to the star.

Given the agreement with the blueshifted TiO_2 emission, the outflow traced by the scattered light is likely oriented out of the plane of the sky. The lack of consistent v_{LSR} coverage over the different TiO_2 transitions, however, further complicates the three-dimensional and kinematic constraints. In-depth analysis of all other emission lines detected with ALMA is needed to constrain the basic properties of the south-west tail.

4.5. Titanium dioxide and dust formation

If the nucleation of TiO_2 can occur at $\lesssim$2000 K (e.g. Lee et al. 2015), one expects TiO_2 depletion from the gas phase initiated close to the star, i.e. within a few stellar radii. From the ALMA observations O+15 put an upper limit to the dust-condensation radius of $\sim 0\farcs06 \pm 0\farcs02 \approx 10$ stellar radii. The TiO_2 emission is present close to the star and out to $\lesssim 0\farcs45$ in directions without extended continuum emission. Where TiO_2 and the bulk dust coexist, the emission extends to $\sim 0\farcs20$, well beyond the dust-condensation radius. Since the TiO_2 emission is seen at radial distances from the star far beyond the dust-condensation region, and along directions where dust continuum is observed, we claim that TiO_2 is not a tracer for low grain-formation efficiency. The strong correspondence between the TiO_2 emission and the south-west tail of dust-scattered stellar light (see Sect. 3.1 and Fig. 2) supports this. We also considered the high derived column density and suggest that TiO_2 plays only a minor role as a primary dust seed around VY CMa.

Since the ALMA observations covered no transitions of TiO, we cannot expand the discussion of K+13a on the relation between TiO, TiO_2, and the dust.

5. Conclusion

We detect 15 transitions of TiO_2 in high-resolution ALMA observations of the red supergiant VY CMa. The main emission region spans $\sim 0\farcs9$ (∼1080 AU) in a roughly east-west oriented direction, centred on the star. The behaviour of the gas is complex throughout v_{LSR}-space with bright peaks appearing only in very confined v_{LSR}-ranges, implying that the outflow is very clumpy, on spatial scales not resolved by the current observations with a $0\farcs23 \times 0\farcs13$ beam. We observe a tail of TiO_2 emission extending out to ∼1″ south-west of the star, consistent with structures seen in the optical and near-infrared. It is oriented out of the plane of the sky and mainly covers projected velocities of a few km s^{-1}, but reaches up to ∼40 km s^{-1} in some cases. We suggest that the TiO_2 in this tail is illuminated by stellar radiation penetrating through a low-density cavity in the south-west part of the circumstellar environment of the star, potentially created by the ejection that led to the south-west clump. Within a bipolar-like TiO_2 outflow, the blue-shifted emission exhibits a strongly different orientation and behaviour than the red-shifted emission, suggesting that the stellar wind runs into the large body of dust situated $\sim 0\farcs335$ (∼400 AU) south-east of the star.

We suggest that TiO_2 might play only a minor role in the dust-condensation process in the complex outflow around VY CMa, and potentially also around other oxygen-rich evolved stars with extreme mass outflows. High-resolution imaging is however still needed to correlate the emission of TiO_2 with that of TiO, and to further investigate the relative importance of silicon, titanium, and other metals in the dust condensation.

Acknowledgements. This paper makes use of the following ALMA data: ADS/JAO.ALMA2011.0.00011.SV. ALMA is a partnership of ESO (representing its member states), NSF (USA) and NINS (Japan), together with NRC (Canada) and NSC and ASIAA (Taiwan), in cooperation with the Republic of Chile. The Joint ALMA Observatory is operated by ESO, AUI/NRAO and NAOJ. W.V. and E.O.G. acknowledge support from the ERC through consolidator grant 614264. M.M. has received funding from the People Programme (Marie Curie Actions) of the EU's FP7 (FP7/2007-2013) under REA grant agreement No. 623898.11.

References

Brünken, S., Müller, H. S. P., Menten, K. M., McCarthy, M. C., & Thaddeus, P. 2008, ApJ, 676, 1367
Cernicharo, J., Spielfiedel, A., Balança, C., et al. 2011, A&A, 531, A103
Chiavassa, A., Freytag, B., Masseron, T., & Plez, B. 2011, A&A, 535, A22
De Beck, E., Decin, L., de Koter, A., et al. 2010, A&A, 523, A18
Decin, L., Hony, S., de Koter, A., et al. 2006, A&A, 456, 549
Gail, H.-P., Wetzel, S., Pucci, A., & Tamanai, A. 2013, A&A, 555, A119
Grein, F. 2007, J. Chem. Phys., 126, 034313
Harper, G. M., Brown, A., & Lim, J. 2001, ApJ, 551, 1073
Houk, N., & Smith-Moore, M. 1988, Michigan Catalogue of Two-dimensional Spectral Types for the HD Stars, Vol. 4, Declinations −26°0 to −12°0 (Ann Arbor: University of Michigan)

Humphreys, R. M., Helton, L. A., & Jones, T. J. 2007, AJ, 133, 2716
Jeong, K. S., Winters, J. M., Le Bertre, T., & Sedlmayr, E. 2003, A&A, 407, 191
Kamiński, T., Gottlieb, C. A., Menten, K. M., et al. 2013a, A&A, 551, A113
Kamiński, T., Gottlieb, C. A., Young, K. H., Menten, K. M., & Patel, N. A. 2013b, ApJS, 209, 38
Keenan, P. C., & McNeil, R. C. 1989, ApJS, 71, 245
Lee, G., Helling, C., Giles, H., & Bromley, S. T. 2015, A&A, 575, A11
Monnier, J. D., Berger, J.-P., Le Bouquin, J.-B., et al. 2014, in SPIE Conf. Ser., 9146, 1
Müller, H. S. P., Thorwirth, S., Roth, D. A., & Winnewisser, G. 2001, A&A, 370, L49
Müller, H. S. P., Schlöder, F., Stutzki, J., & Winnewisser, G. 2005, J. Mol. Struct., 742, 215
Muller, S., Dinh-V-Trung, Lim, J., et al. 2007, ApJ, 656, 1109
Nittler, L. R., & Alexander, C. M. O. 1999, in 30th Annual Lunar and Planetary Science Conference, 2041
Nuth, III, J. A., & Ferguson, F. T. 2006, ApJ, 649, 1178
O'Gorman, E., Vlemmings, W., Richards, A. M. S., et al. 2015, A&A, 573, L1
Richards, A. M. S., Impellizzeri, C. M. V., Humphreys, E. M., et al. 2014, A&A, 572, L9
Shenoy, D. P., Jones, T. J., Humphreys, R. M., et al. 2013, AJ, 146, 90
Smith, N., Humphreys, R. M., Davidson, K., et al. 2001, AJ, 121, 1111
Wang, H., Steimle, T. C., Apetrei, C., & Maier, J. P. 2009, Phys. Chem. Chem. Phys., 11, 2649
Zhang, B., Reid, M. J., Menten, K. M., & Zheng, X. W. 2012, ApJ, 744, 23
Ziurys, L. M., Milam, S. N., Apponi, A. J., & Woolf, N. J. 2007, Nature, 447, 1094

Pages 8 to 24 are available in the electronic edition of the journal at http://www.aanda.org

Appendix A: Maps of titanium dioxide emission

Figures A.1 to A.15 show channel maps of the detected TiO_2 emission lines (Table 2, Fig. 1) at a velocity resolution of 2 km s^{-1}, covering the range $-14 \leq v_{LSR} \leq 78$ km s^{-1}. This v_{LSR}-range covers the bulk of all TiO_2 emission; emission at more extreme velocities is no longer visible in the channel maps. Figure A.16 shows integrated-intensity maps for all listed lines, covering the v_{LSR}-ranges indicated in Table 2. Figure A.17 shows a comparison of the TiO_2 line emission to the south-west tail detected at 310.78 GHz, which is discussed in Sects. 3.1 and 4.4.

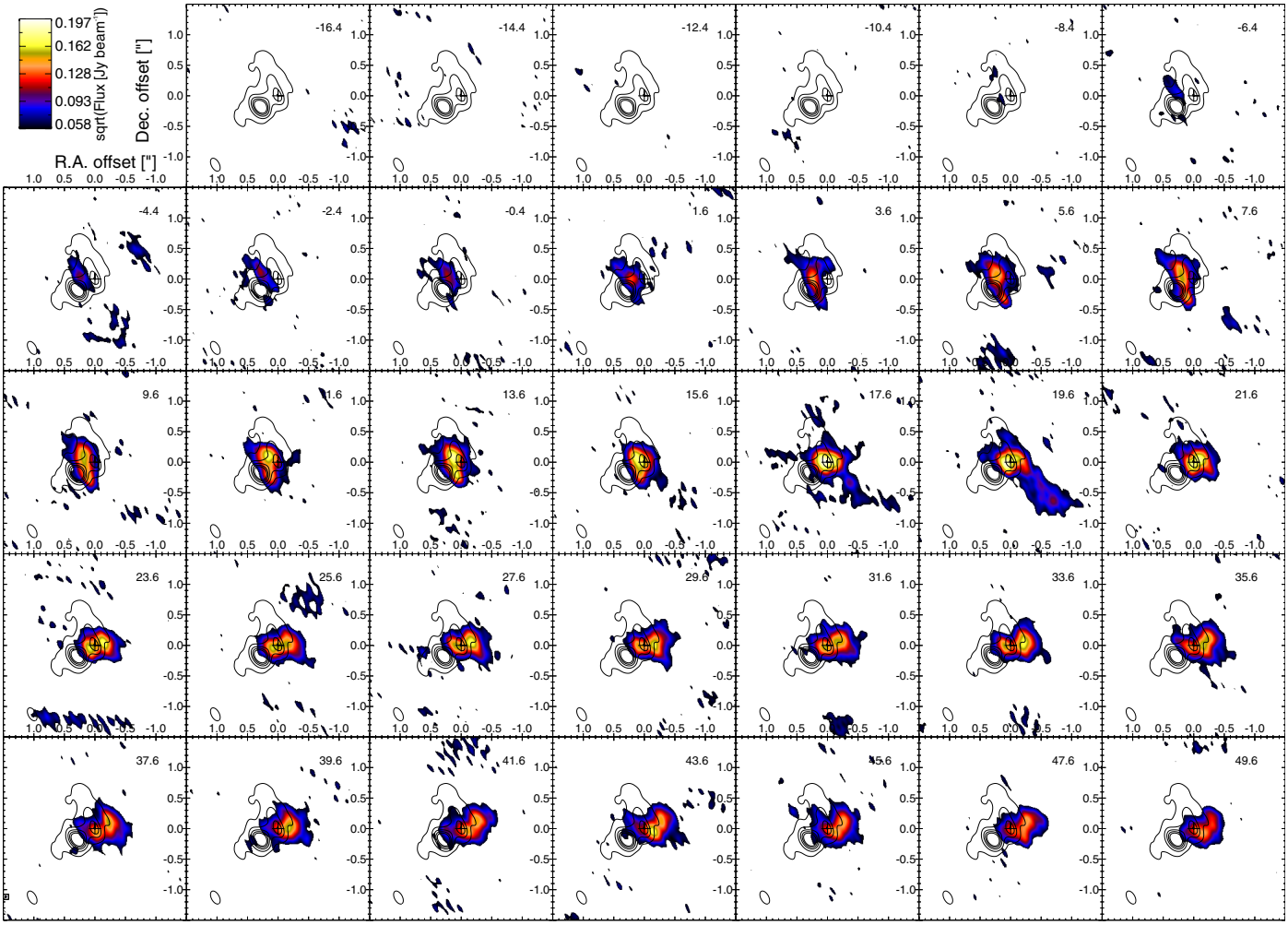

Fig. A.1. Channel maps of the TiO_2 emission at 310.55 GHz, at a 2 km s^{-1} velocity resolution. Black contours show the continuum measured with ALMA at 321 GHz (O+15; R+14). The stellar position is indicated with a white cross. Spatial scales are indicated in the *top left panel* and are the same for all panels. The colour scale starts at the 3σ level and is plotted as the square root of the flux for increased contrast.

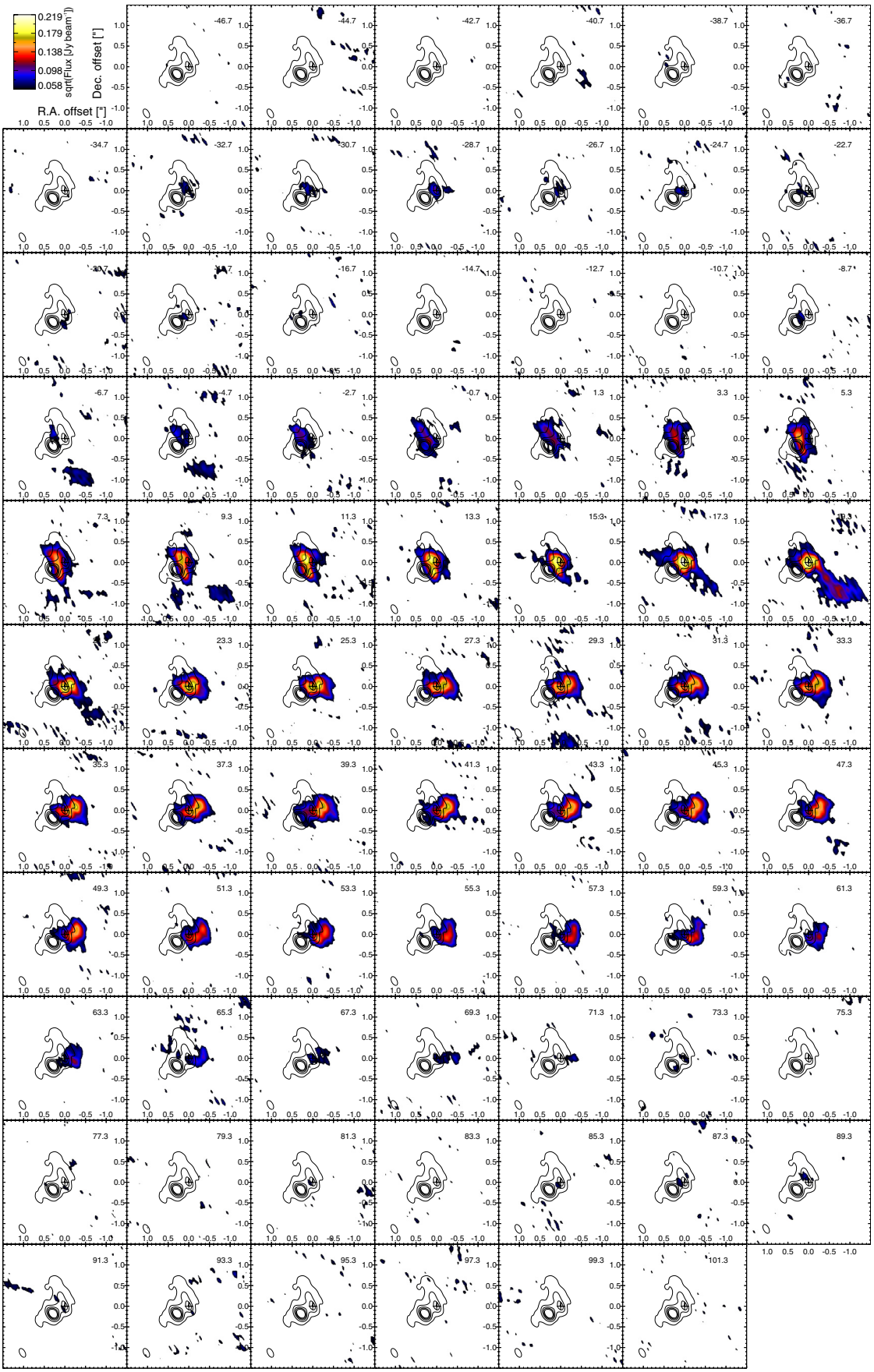

Fig. A.2. Same as Fig. A.1, but for TiO_2 emission at 310.78 GHz.

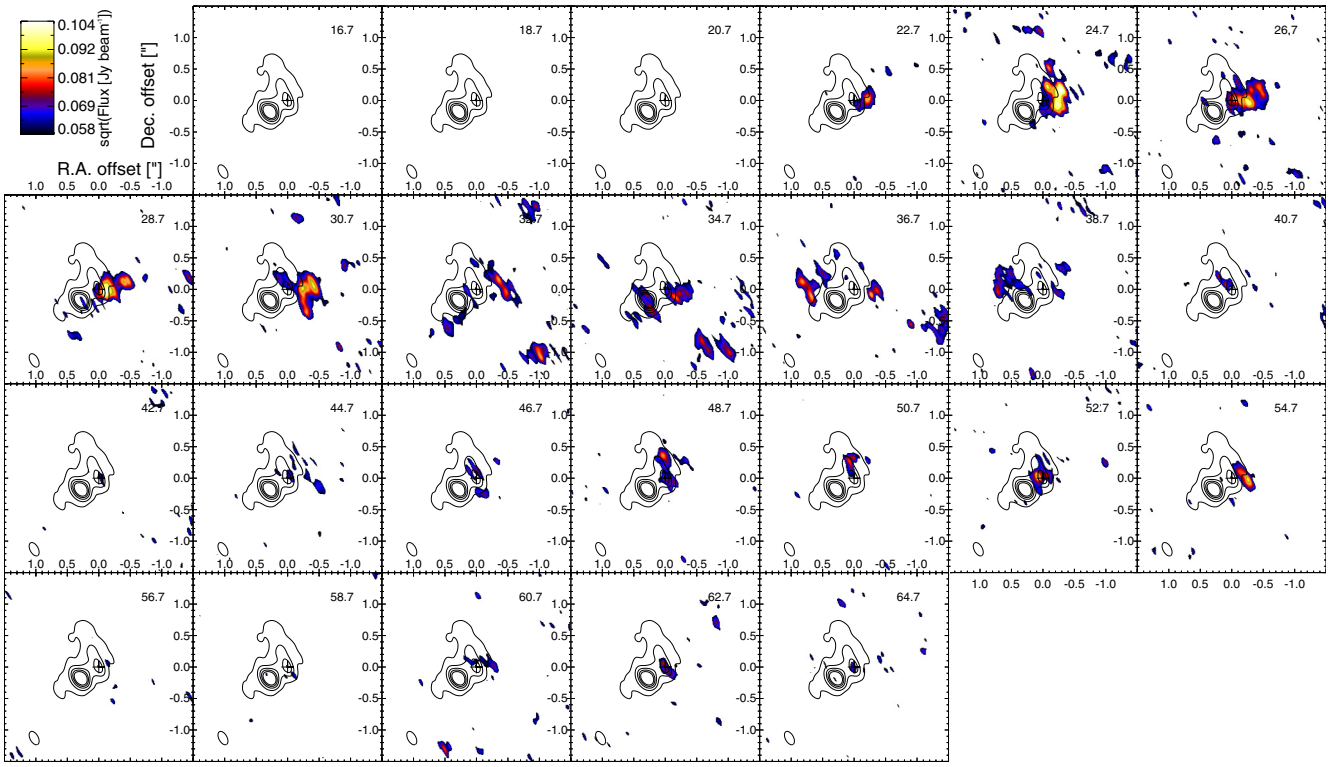

Fig. A.3. Same as Fig. A.1, but for TiO_2 emission at 311.46 GHz.

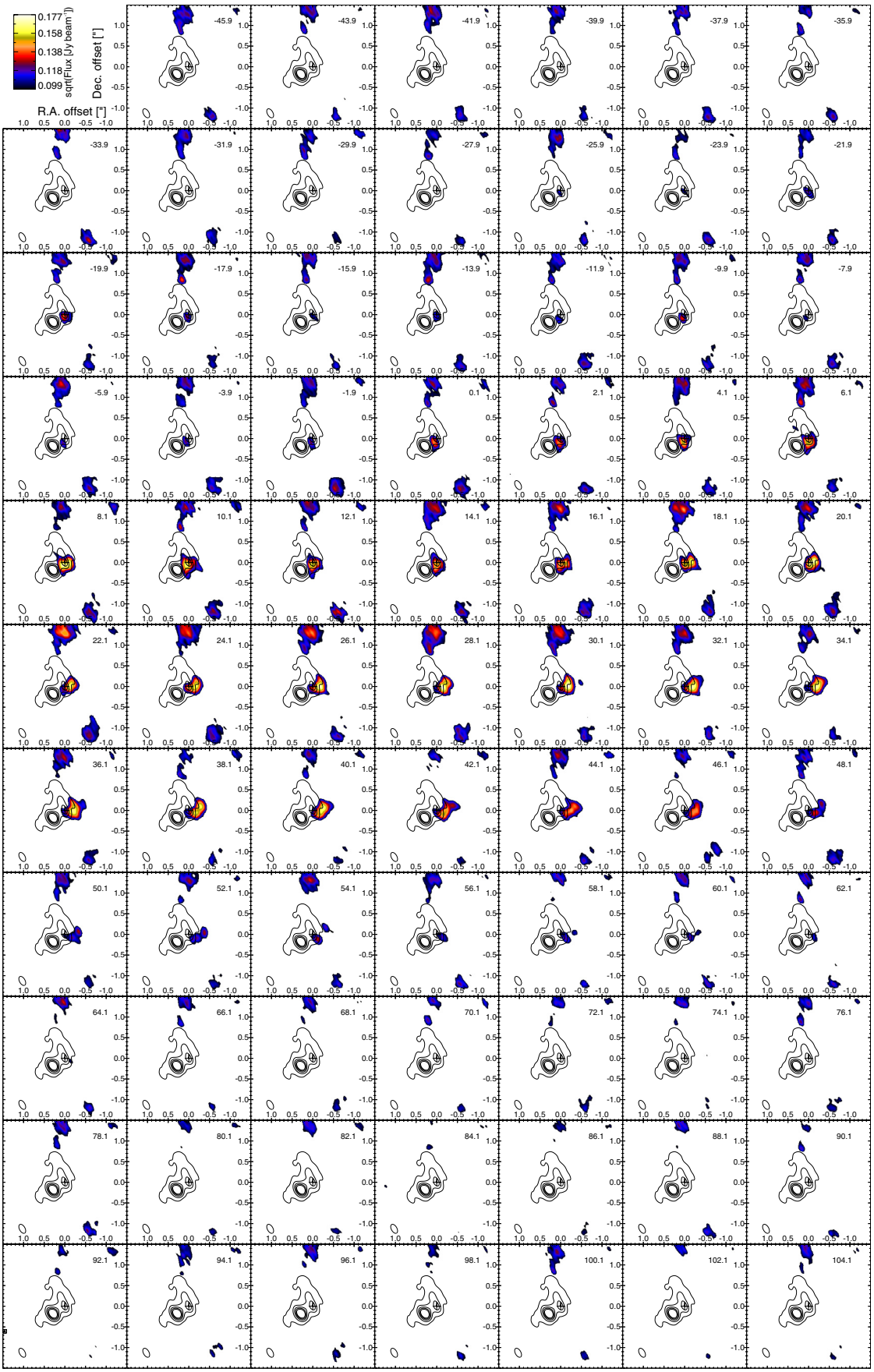

Fig. A.4. Same as Fig. A.1, but for TiO_2 emission at 312.25 GHz.

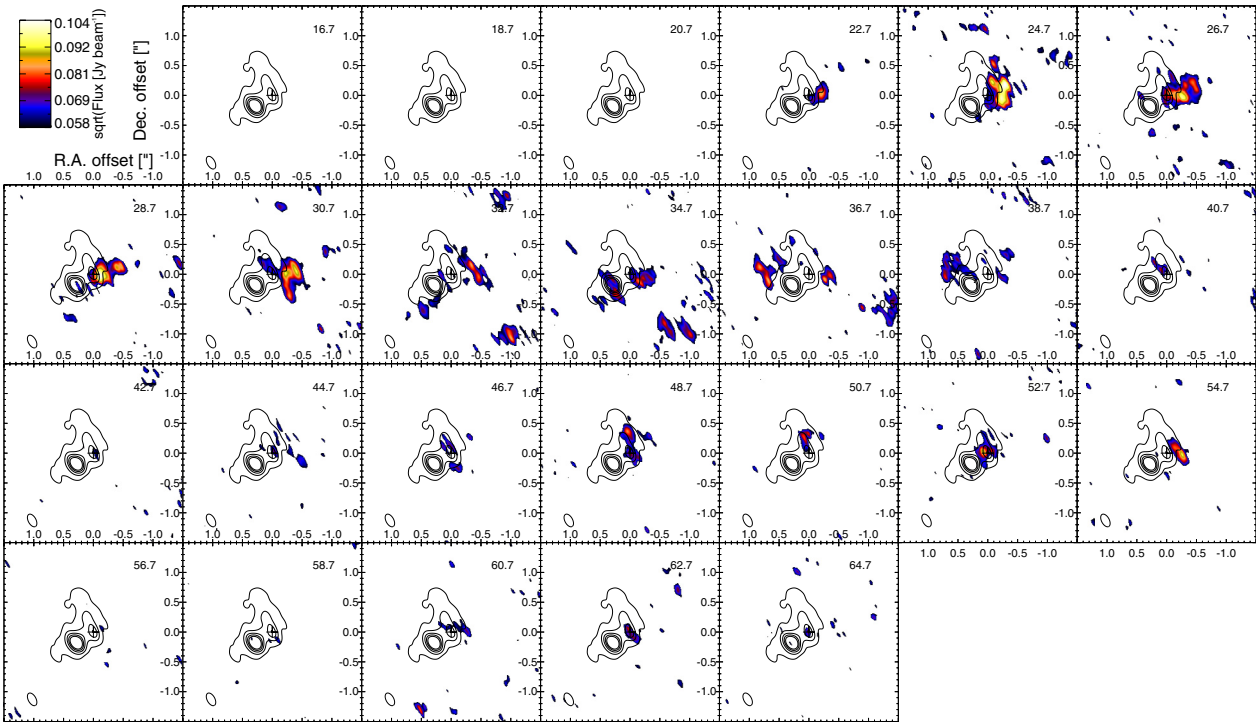

Fig. A.5. Same as Fig. A.1, but for TiO_2 emission at 312.73 GHz.

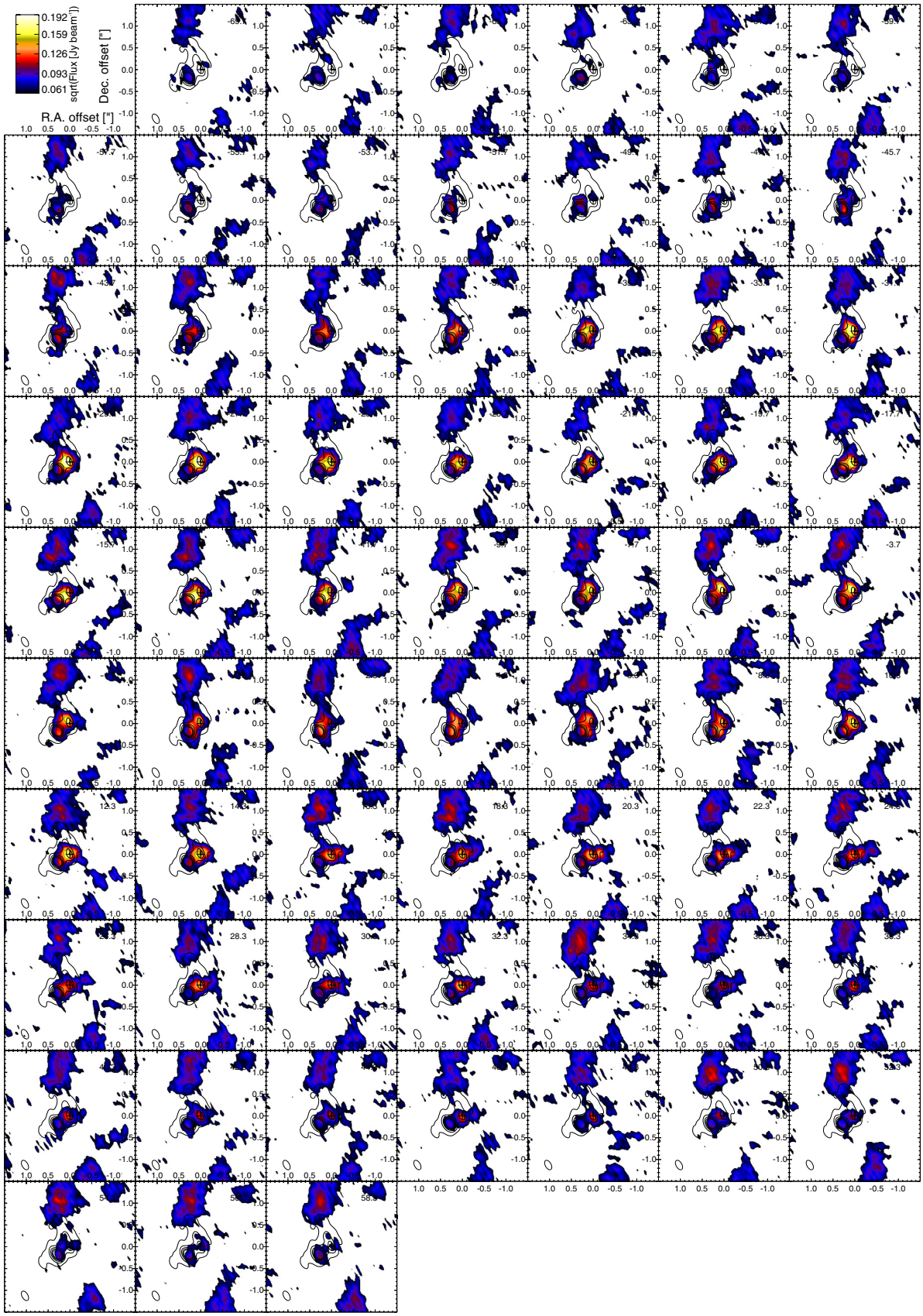

Fig. A.6. Same as Fig. A.1, but for TiO_2 emission at 312.82 GHz.

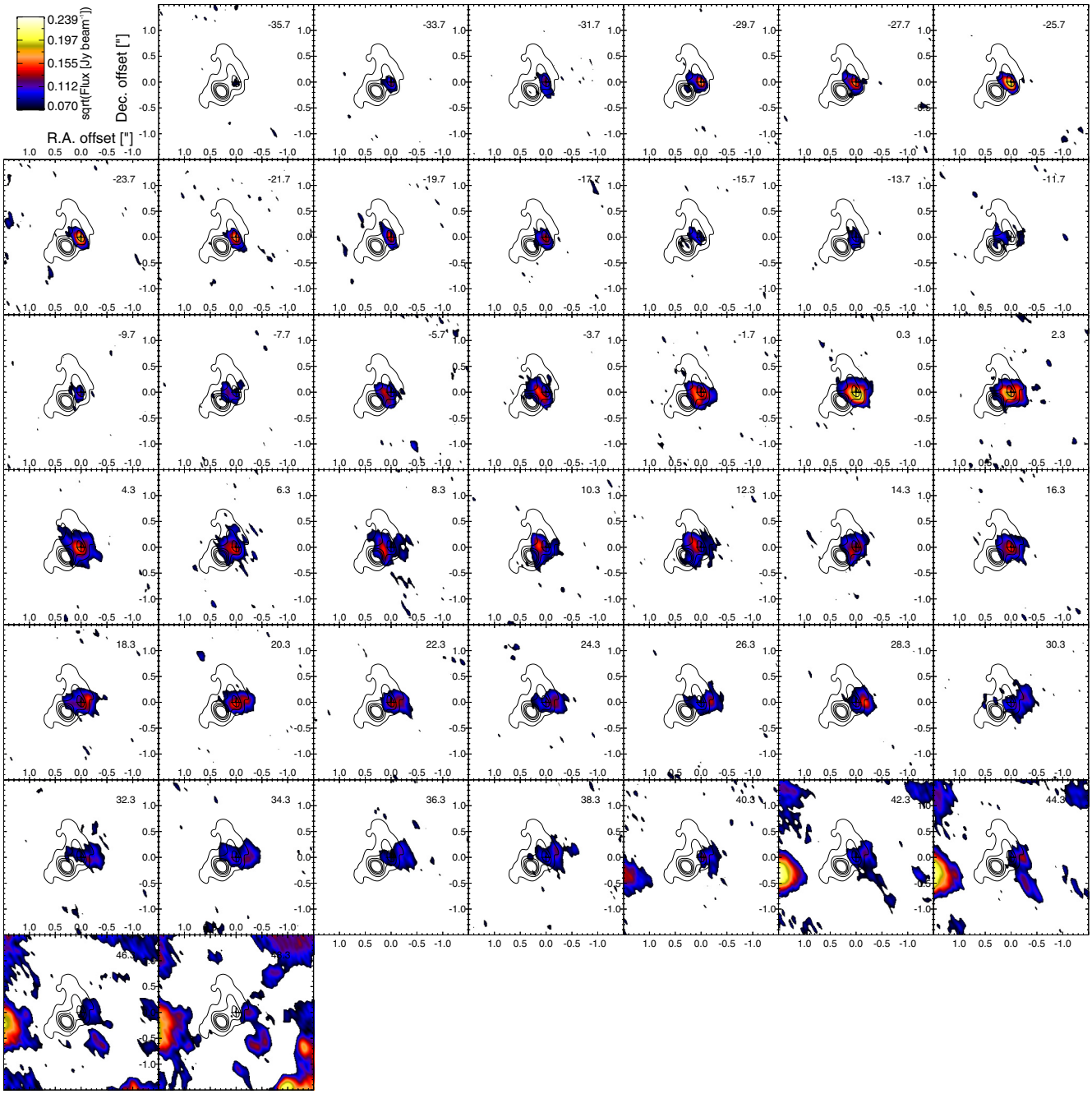

Fig. A.7. Same as Fig. A.1, but for TiO_2 emission at 321.40 GHz. Artefacts in channels with $v_{LSR} \geq 55$ km s^{-1} are due to the presence of strong SO_2 emission. See also Fig. 1.

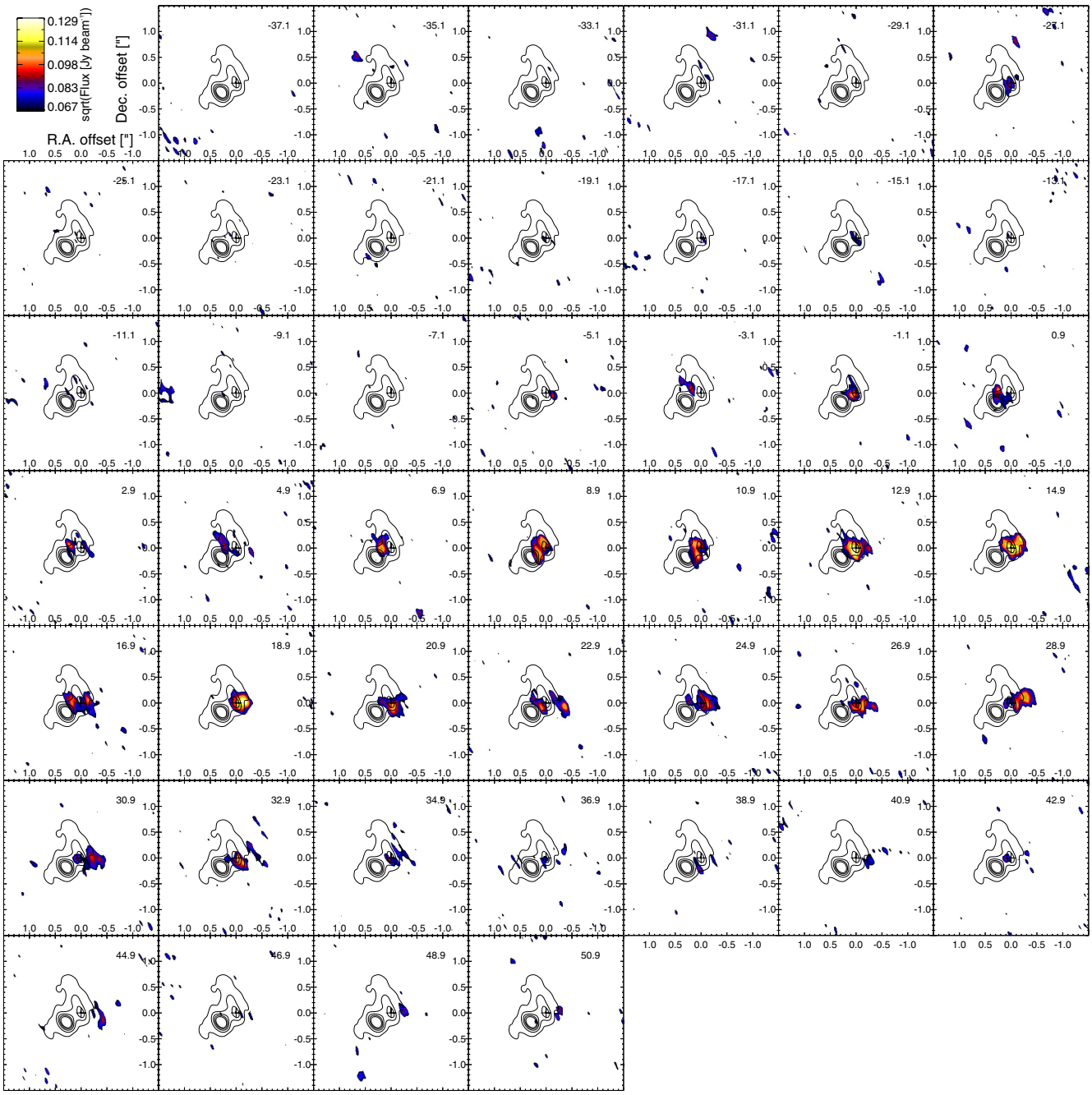

Fig. A.8. Same as Fig. A.1, but for TiO_2 emission at 321.50 GHz.

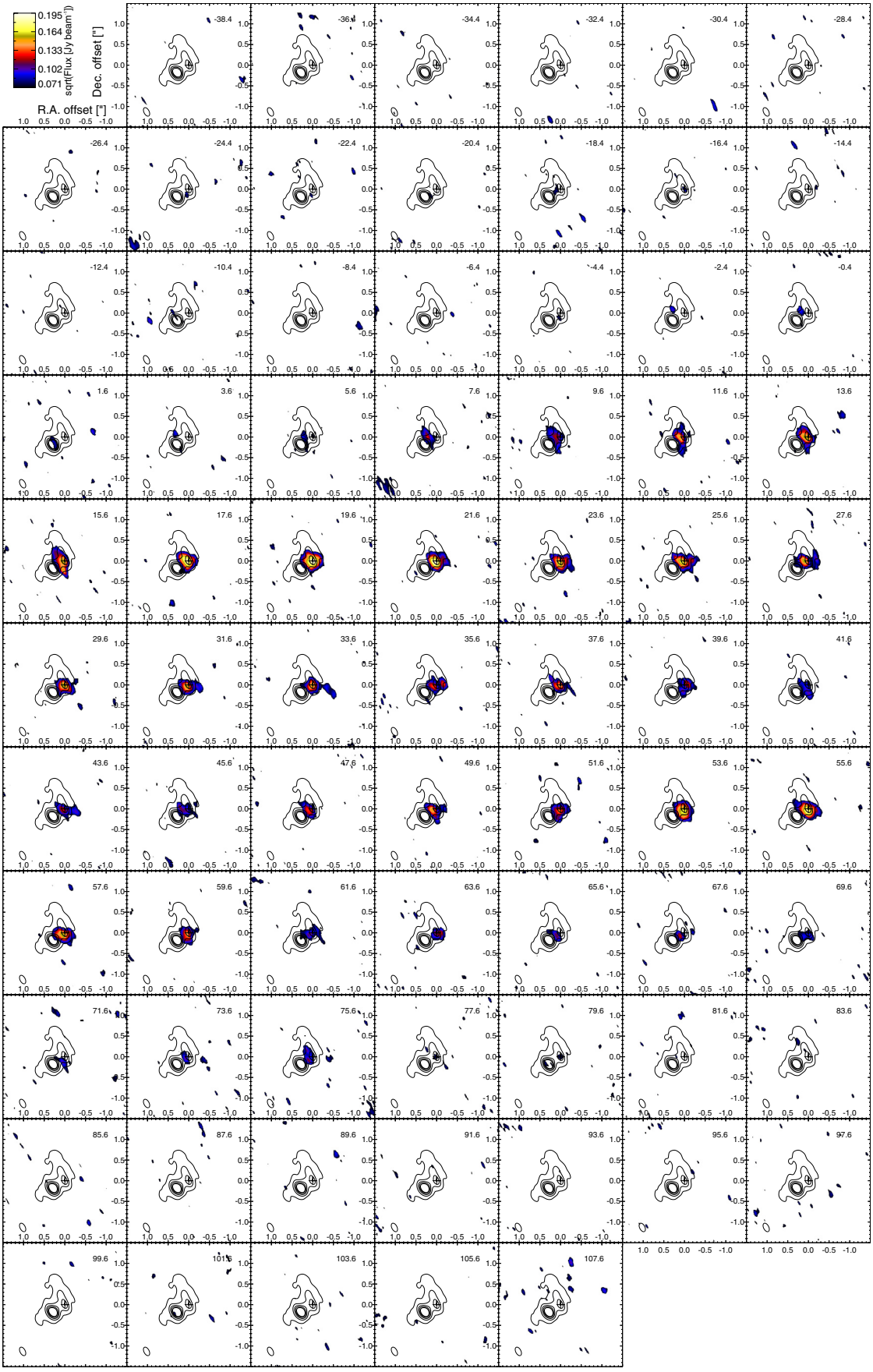

Fig. A.9. Same as Fig. A.1, but for TiO_2 emission at 322.33 GHz.

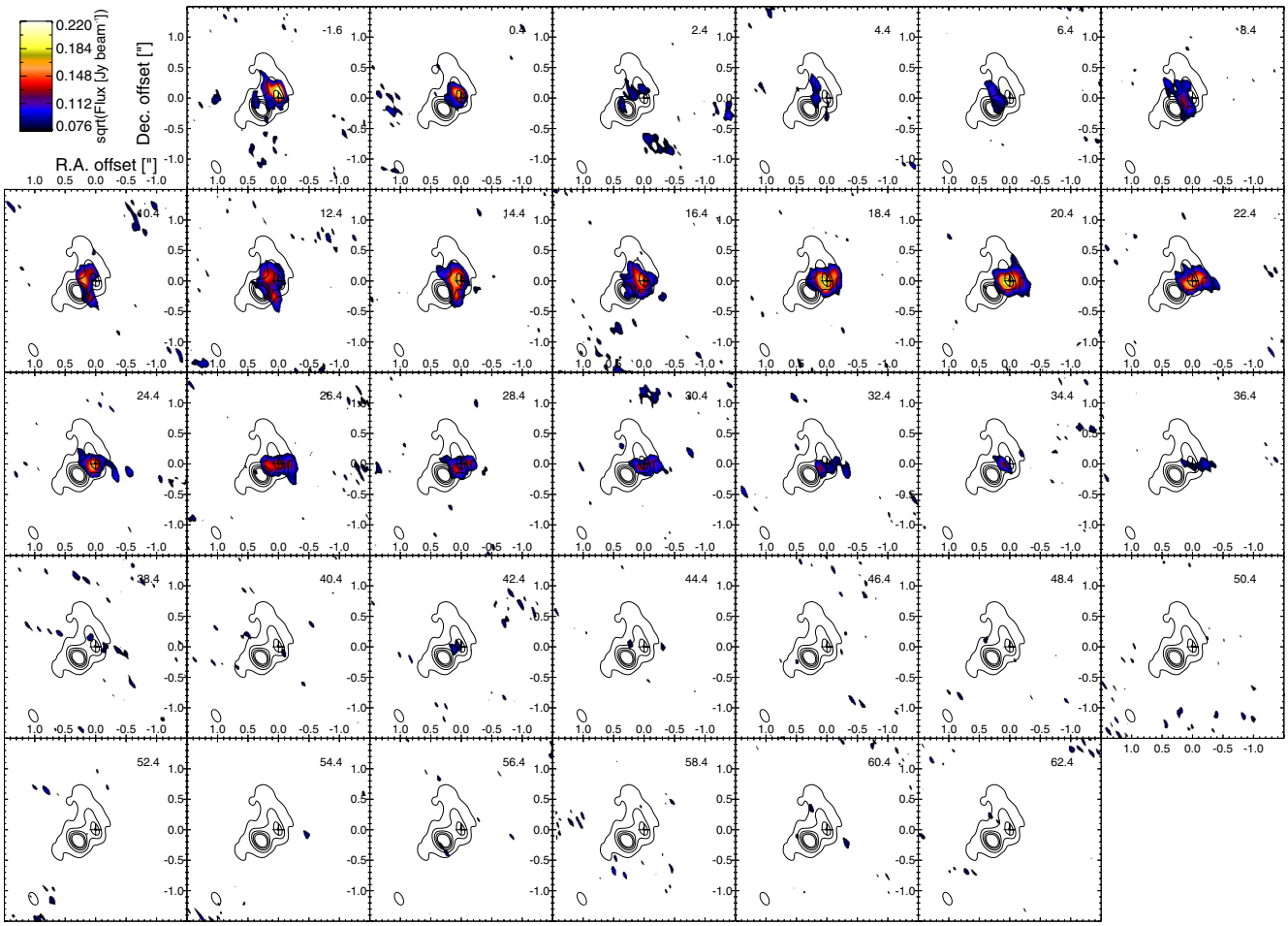

Fig. A.10. Same as Fig. A.1, but for TiO_2 emission at 322.61 GHz.

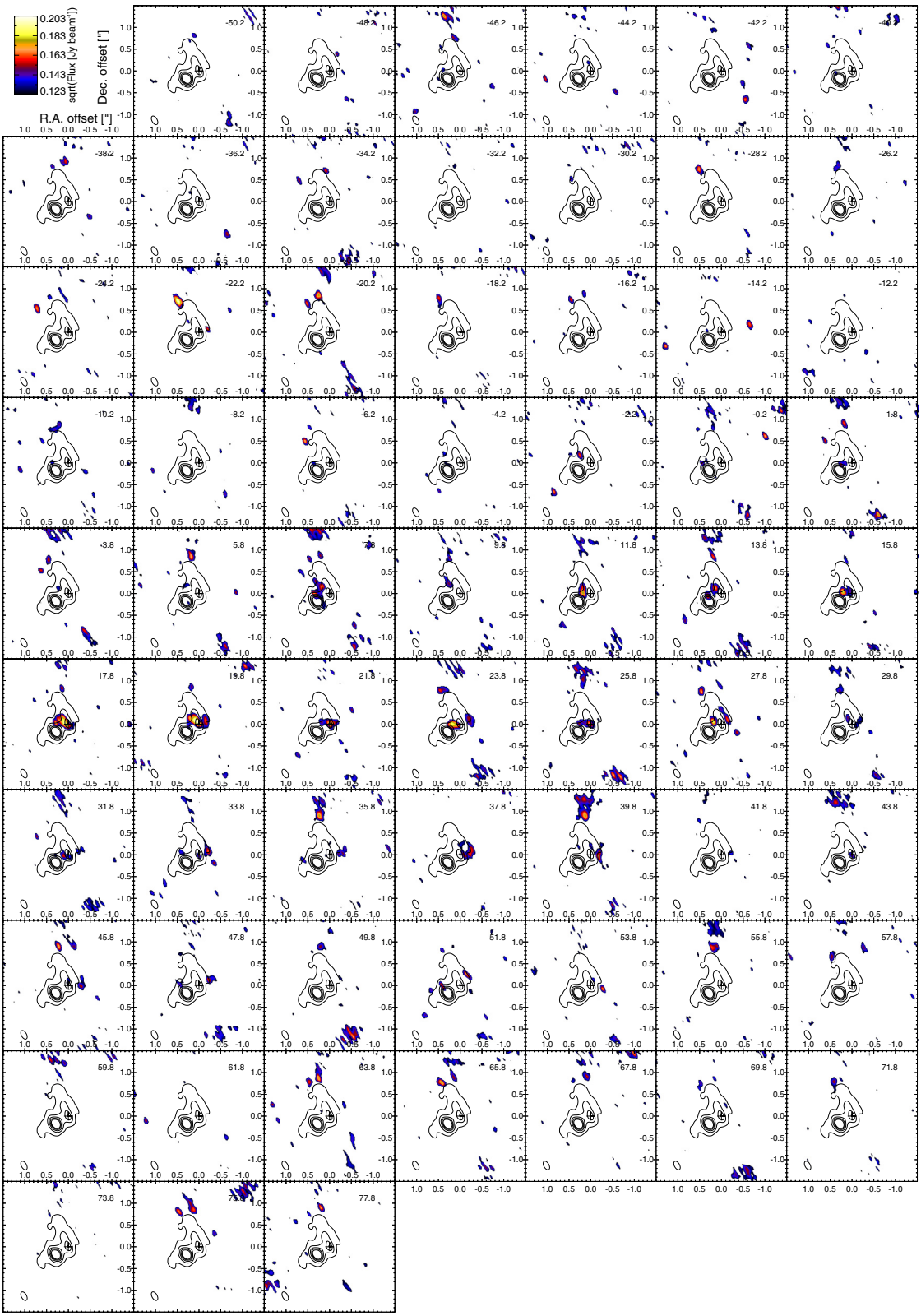

Fig. A.11. Same as Fig. A.1, but for TiO_2 emission at 324.49 GHz.

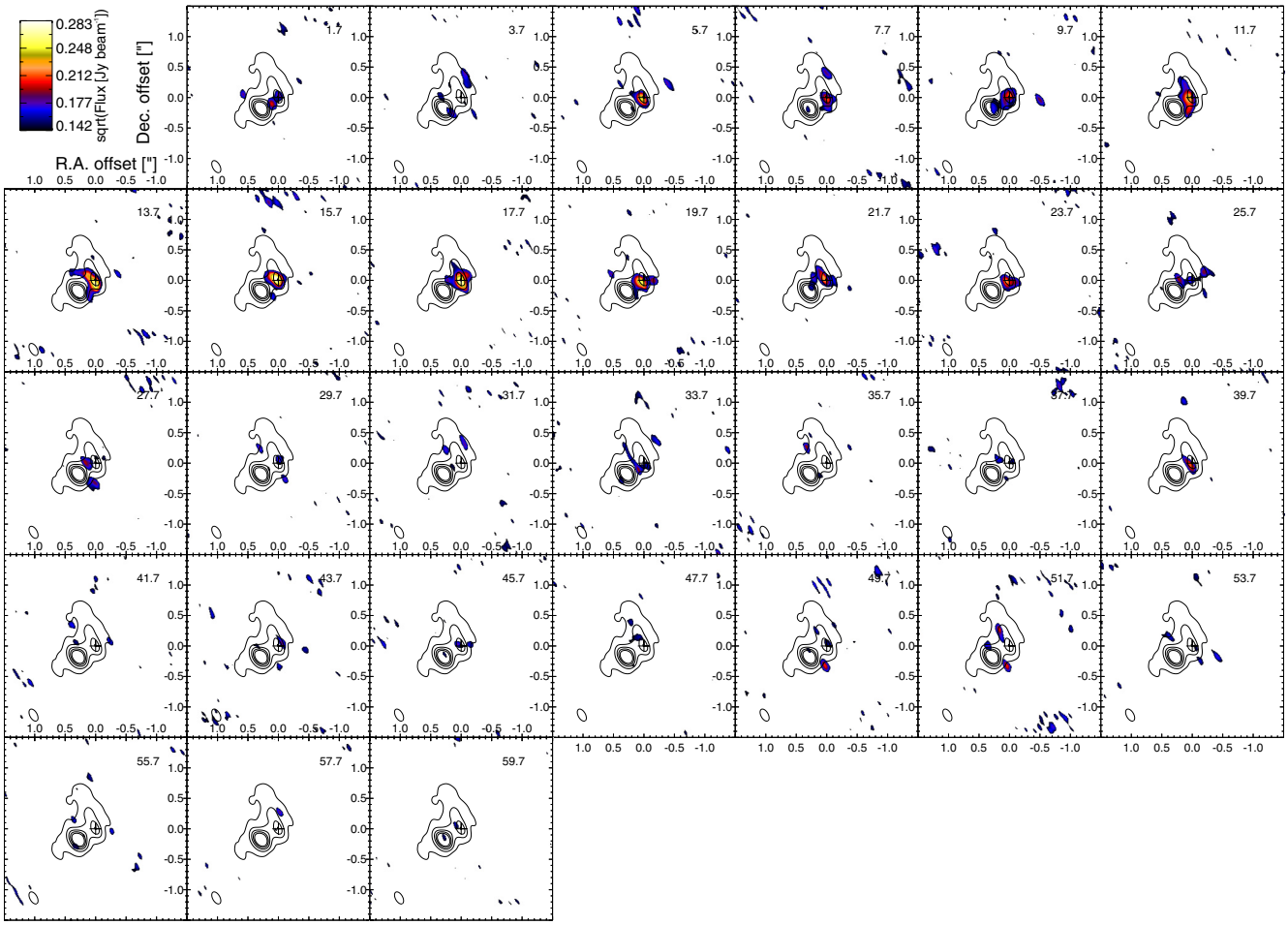

Fig. A.12. Same as Fig. A.1, but for TiO_2 emission at 324.96 GHz.

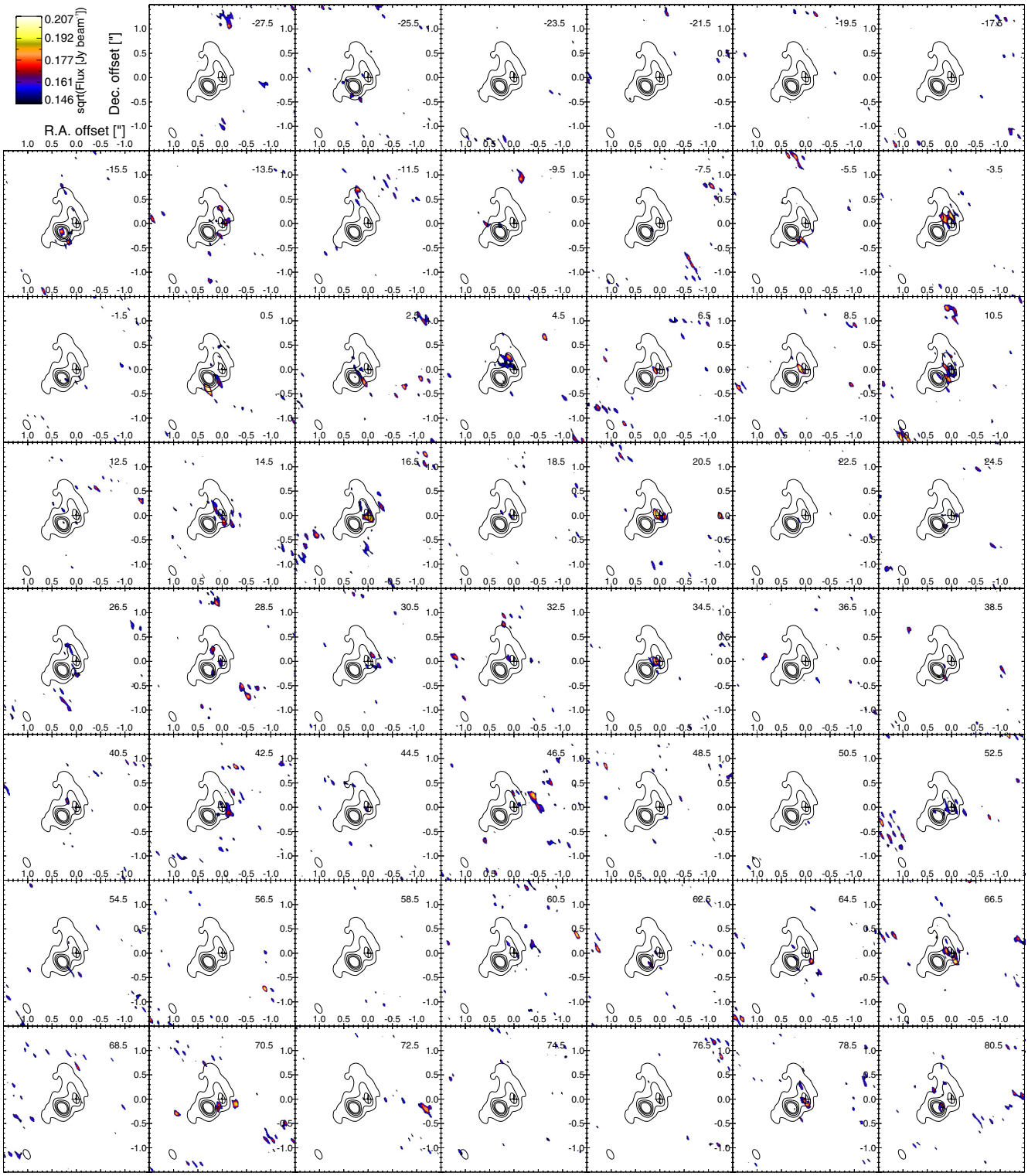

Fig. A.13. Same as Fig. A.1, but for TiO_2 emission at 325.32 GHz.

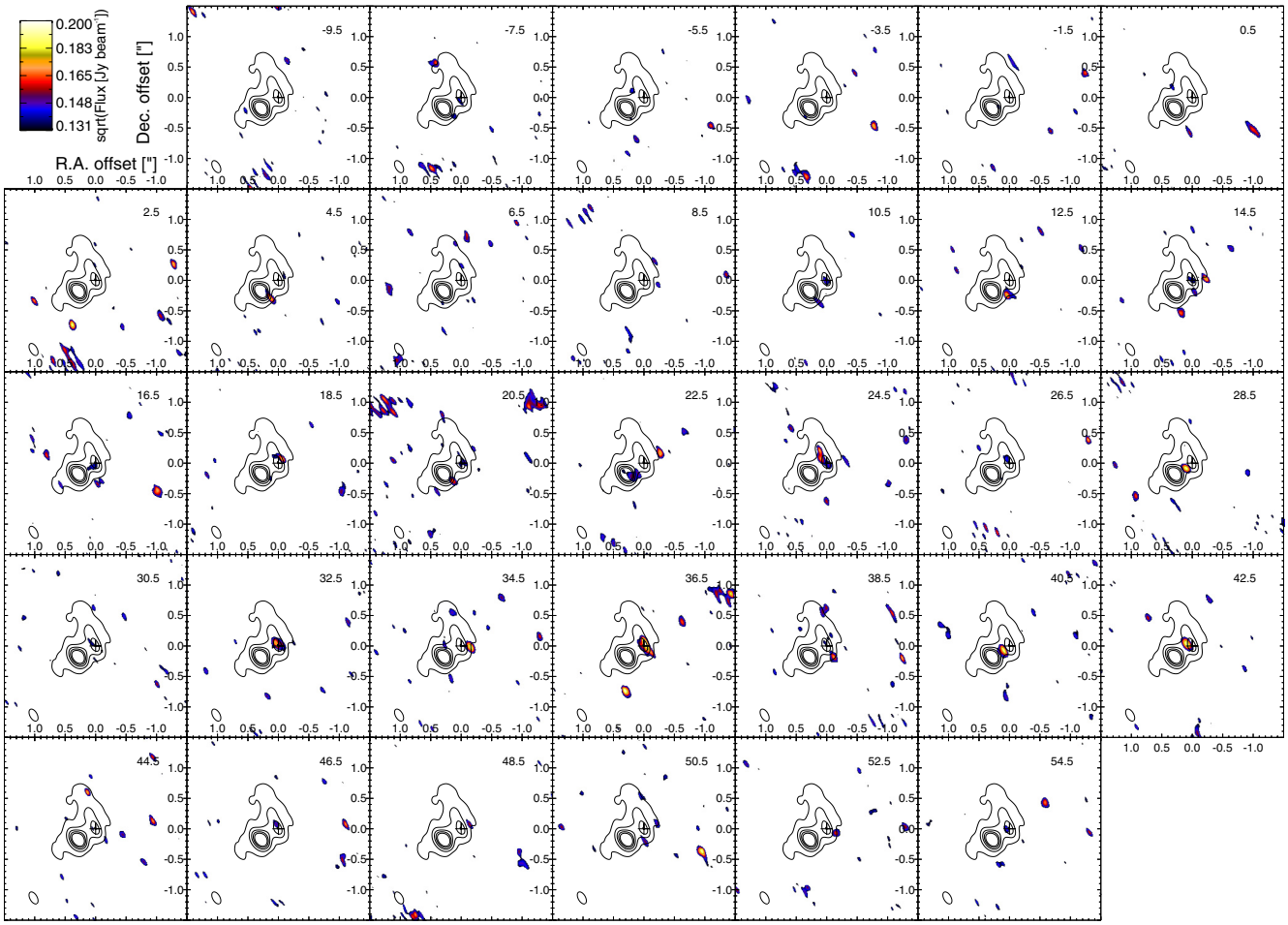

Fig. A.14. Same as Fig. A.1, but for TiO_2 emission at 325.50 GHz.

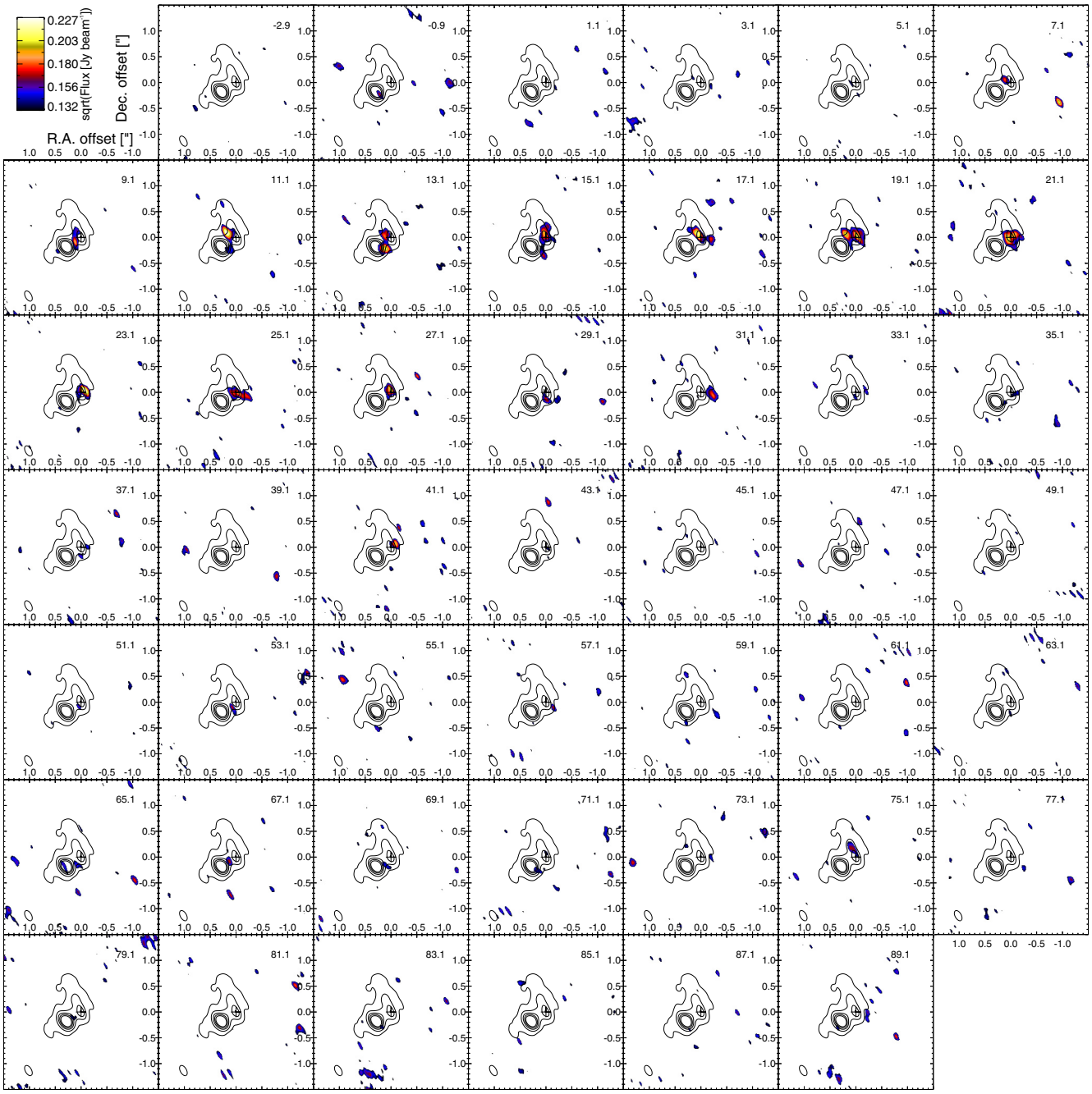

Fig. A.15. Same as Fig. A.1, but for TiO_2 emission at 325.60 GHz.

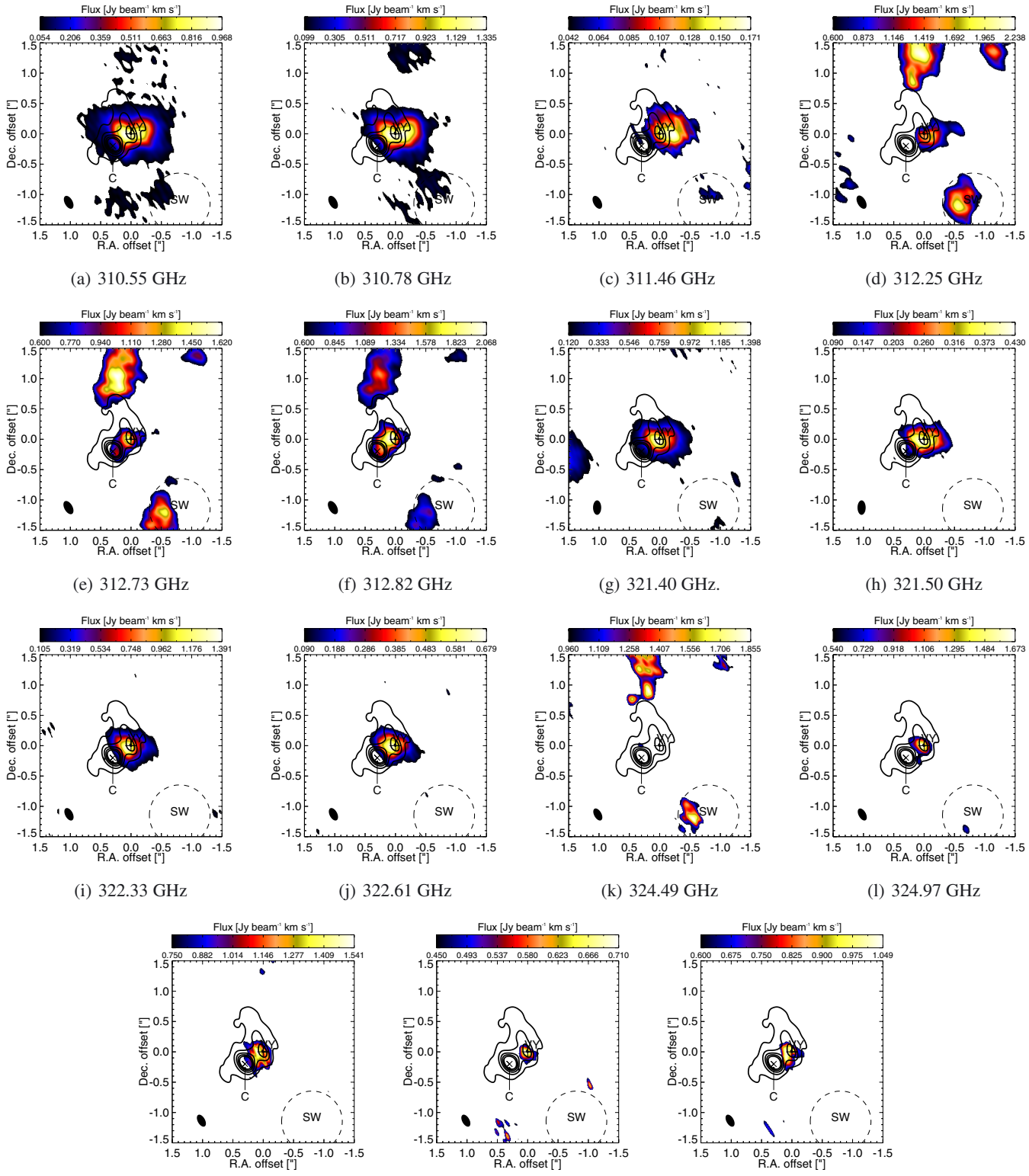

(a) 310.55 GHz (b) 310.78 GHz (c) 311.46 GHz (d) 312.25 GHz

(e) 312.73 GHz (f) 312.82 GHz (g) 321.40 GHz. (h) 321.50 GHz

(i) 322.33 GHz (j) 322.61 GHz (k) 324.49 GHz (l) 324.97 GHz

(m) 325.32 GHz (n) 325.50 GHz (o) 325.60 GHz

Fig. A.16. Integrated-intensity maps of TiO_2 emission. Colour maps show the intensity integrated over the v_{LSR}-ranges indicated in Table 2 and Fig. 1 and cut off at 3σ. Contours show the ALMA 321 GHz continuum. Labels indicate the positions of the star (+, VY) and the continuum component (x, C) to the south-east (O+15; R+14), and the position and approximate extent of the south-west clump of Shenoy et al. (2013, SW and a dashed 1″ diameter circle). The presence of cleaning artefacts, mainly at ~312 GHz, is addressed in Sect. 2.

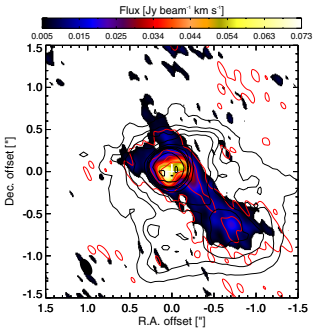

(a) TiO_2 at 310.55 GHz

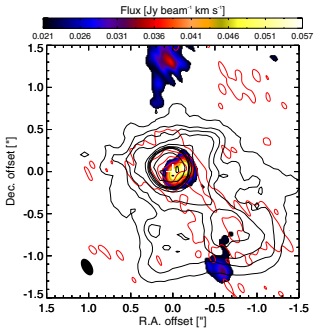

(b) TiO_2 at 312.25 GHz

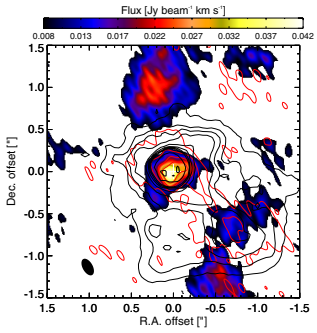

(c) TiO_2 at 312.73 GHz

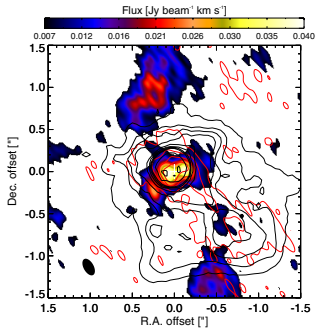

(d) TiO_2 at 312.82 GHz

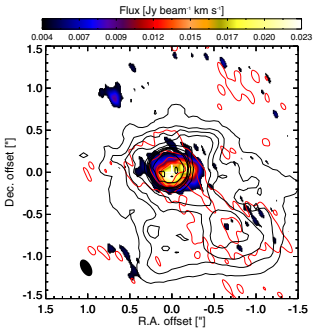

(e) TiO_2 at 321.40 GHz.

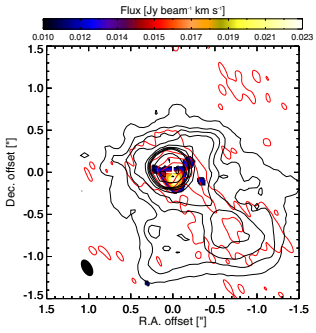

(f) TiO_2 at 321.50 GHz

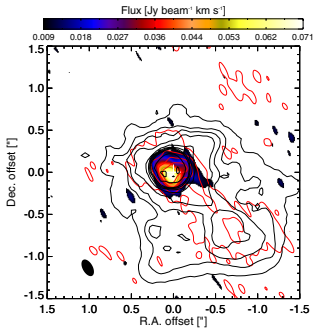

(g) TiO_2 at 322.33 GHz

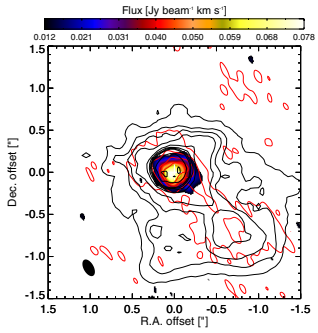

(h) TiO_2 at 322.61 GHz

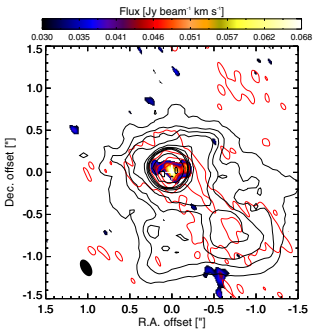

(i) TiO_2 at 324.49 GHz

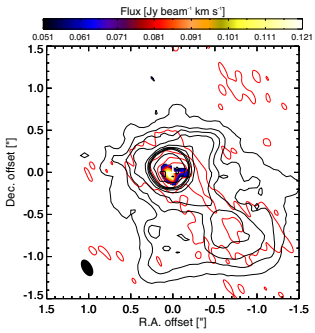

(j) TiO_2 at 324.97 GHz

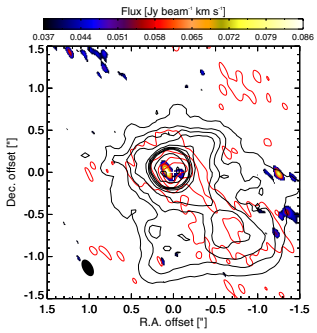

(k) TiO_2 at 325.32 GHz

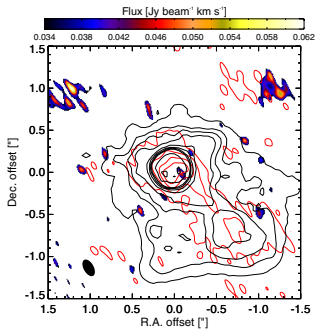

(l) TiO_2 at 325.50 GHz

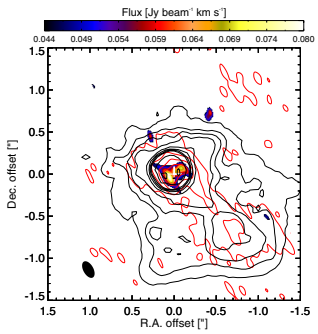

(m) TiO_2 at 325.60 GHz

Fig. A.17. Comparison of TiO_2 emission lines listed in Table 2 to south-west tail at 310.78 GHz (red contours) and HST image (black contours). Emission integrated over $19 \leq v_{LSR} \leq 22$ km s^{-1} plotted at $>3\sigma$ (colour scale). Emission of 311.46 GHz was omitted since the relevant v_{LSR}-range is not covered by the observations.